

- 1 This manuscript is a **preprint** accepted for publication in *Tectonics*. We welcome feedback and invite
- 2 you to contact the authors directly to comment on the manuscript.

3 Taking the pulse of salt-detached gravity 4 gliding in the eastern Mediterranean

5 **Sian L. Evans^{1,2}, Christopher A.-L. Jackson^{1,3} and Davide Oppo⁴**

6 ¹ Basins Research Group (BRG), Department of Earth Science & Engineering, Imperial
7 College, London, UK

8 ² Present address: Department of Geosciences, University of Oslo, Oslo, Norway

9 ³ Present address: Department of Earth and Environmental Sciences, The University of
10 Manchester, Manchester, UK

11 ⁴ Sedimentary Basins Research Group, School of Geosciences, University of Louisiana at
12 Lafayette, Lafayette, USA

13 Corresponding author: Sian L. Evans (sian.lianne@outlook.com)

14 **Key Points:**

- 15 • Ramp syncline basins (RSBs) offshore Lebanon are excellent records of salt-detached
16 horizontal translation dominated by gravity-gliding
- 17 • Rates of basinward translation are approximately uniform at the km-scale, but show
18 significant lateral variability at the margin-scale
- 19 • Differential translation rates are predominantly controlled by 'pulses' of salt flow due to
20 volumetric flux imbalances, as well as the overburden mechanics

21 Abstract

22 Despite having a profound impact on the structural evolution of salt-influenced basins, spatial and
23 temporal variations in rates of salt flow, and their key controls, remain largely unconstrained. We
24 investigate early-stage salt-detached gliding using a 3D seismic dataset from the Levant Margin in the
25 Eastern Mediterranean, where gravitational instability due to margin uplift has caused north-
26 westward translation of the Messinian salt sheet and its overburden. Large base-salt anticlines mean
27 that basinward translation is recorded by the development of supra-salt ramp syncline basins (RSBs)
28 and fluid escape pipes, the latter forming due to the leakage of fluid from the anticline crests. The
29 trails of pipes provide kinematic vectors of transport direction, while the stratigraphic record of the
30 RSBs not only constrains the relative ages of the pipes, but allows us to quantify the magnitude and
31 approximate rate of translation. We correlate intra-RSB horizons across the margin to analyse lateral
32 variations in translation rate, and how these vary through time. We show that translation rates are
33 broadly uniform on the length-scale of individual anticlines (c. 10 km), but that there is significant
34 margin-scale (c. 100 km) lateral variability in both the direction and magnitude of translation. We
35 attribute temporal variations in local rates of translation to cyclical 'pulses' of salt flow due to
36 volumetric flux imbalances across the anticlines, while the distribution of elastic strain in the
37 overburden modulates the overall basin-scale trend. These results demonstrate the importance of
38 local stresses in controlling the local direction and rate of salt flow, and further our understanding of
39 salt and overburden rheology.

40 1 Introduction

41 Salt-influenced basins and passive margins are structurally complex, globally distributed, and
42 hydrocarbon-rich. The variety of structural styles in different salt basins around the world is testament
43 to the myriad of ways in which salt-related deformation can affect the tectono-stratigraphic evolution
44 of sedimentary basins. Over the past few decades seismic reflection data have transformed our
45 understanding of subsurface salt tectonics, allowing us to investigate the regional structural evolution
46 of salt basins (Jackson et al., 1994; Hudec and Jackson, 2007; Jackson and Hudec, 2017). However, the
47 various controls on the evolution of these stress-sensitive systems are still debated. Gravity gliding
48 and spreading are simplified end-member models used to describe gravitationally-driven salt tectonics
49 along passive margins (e.g. Brun and Fort, 2011; Peel, 2014; Schultz-Ela, 2001), but the effects of other
50 variables that introduce further complexity into the system, such as base-salt relief (e.g. Dooley et al.,
51 2017; Pichel et al., 2019; Evans and Jackson, 2020a) and intrasalt heterogeneity (e.g. Albertz and Ings,
52 2012; Raith et al., 2016; Rowan et al., 2019), remain poorly understood.

53 Due to the internally chaotic and low-amplitude appearance of salt bodies in seismic reflection data
54 (Jones and Davison, 2014), the deformation history of seismically-imaged salt structures is commonly
55 reconstructed using stratigraphic relationships and structures in the overburden (e.g. Quirk et al.,
56 2012). While this approach is invaluable in reconstructing vertical salt movements (e.g. diapir growth),
57 it often neglects that overburden structures may have also been laterally translated tens of km
58 downdip. Estimations of lateral translation on salt-detached margins have relied heavily on summing
59 extensional fault heaves (in the updip domain) and/or line-length balancing techniques (see Coleman
60 et al., 2017). Typically, the 'undeformed' translational domain has yielded little information of use in
61 this regard (Schultz-Ela, 2001).

62 Ramp syncline basins (RSBs) are one of the few stratigraphic features that record, and thus allow us
63 to quantify, basinward translation of salt overburden (Jackson and Hudec, 2005). Although they were
64 first recognised in the Gulf of Lyon, offshore France more than two decades ago (e.g. Benedicto et al.,
65 1999), they are still often overlooked and under-utilised in many basins (Pichel et al., 2018). Salt-
66 detached RSBs form as a result of salt and overburden translation across a sub-salt topographic high
67 (Fig. 1) (Marton et al., 2000; Jackson and Hudec et al., 2005; Pichel et al., 2018; Evans and Jackson,
68 2020a). This creates a local sediment depocentre adjacent to the high, above its downdip flank (Fig.
69 1). Syn-kinematic strata thicken into this accommodation, and onlap towards the updip high (Fig. 1).
70 As translation continues, the onlapping growth strata are progressively transported away from the
71 high in the direction of salt flow (Fig. 1). This creates an 'onlap surface' in the stratigraphic record, with
72 the horizontal distance from the first onlap to the sub-salt high giving the total magnitude of

73 translation (Fig. 1) (Jackson and Hudec, 2005). Recent studies have begun to exploit the uses of RSBs
74 as records of translation on salt-influenced passive margins, demonstrating how stacked RSBs of
75 different ages may be used to reconstruct the history of salt-detached gravity gliding offshore Brazil
76 (Pichel et al., 2018) and offshore Angola (Evans and Jackson, 2020a).

77 Transient markers such as fluid escape pipes may also record horizontal translation on salt-influenced
78 passive margins (Cartwright et al., 2018; Kirkham et al., 2019). A study of a series of pipes in the deep
79 Levantine Basin, offshore Lebanon, determined that they all originated from a single sub-salt anticline
80 (termed the Oceanus structure; Fig. 2). Each pipe formed vertically above the anticline crest, releasing
81 pressure accumulated in the sub-salt trap in a single event, before being passively translated
82 basinward due to gravity gliding (Fig. 1) (Cartwright et al., 2018). All pipes are thought to be inactive
83 fluid pathways once they are translated away from the anticline crest. The sub-salt trap then recharges
84 until it once again exceeds the critical pressure required for the fluids to hydro-fracture the overlying
85 salt and generate a new fluid escape pipe (Fig. 1) (Cartwright et al., 2018; Oppo et al., 2021). This
86 creates a trail of pipes that record the progressive basinward translation of the overburden
87 (Cartwright et al., 2018). By treating the pipes as direct kinematic indicators the authors estimate the
88 velocity of the overburden and viscosity of the deforming salt sheet (Cartwright et al., 2018). A
89 subsequent study then interpreted four distinct pipe trails originating from a single anticline nearby
90 (termed the Saida-Tyr structure; Fig. 2) (Kirkham et al., 2019). However, both studies are forced to
91 make assumptions about the ages of the pipes, and they are limited to relatively small areas (each <35
92 km²) due to the distribution of pipes, thus giving only local constraints on the kinematics of a much
93 larger salt layer.

94 In this study we apply a new approach to investigating gravity-driven salt translation at the margin-
95 scale (covering an area of c. 5000 km²), integrating the geological records given by RSBs and trails of
96 fluid escape pipes. The young Messinian (latest Miocene) evaporite sequence of the Mediterranean
97 Basin provides a perfect natural laboratory to study active, early-stage, gravity-driven salt tectonics of
98 a thick salt sheet. We analyse eight RSBs and twelve associated fluid escape pipe trails in the updip
99 domain of the northern Levantine Basin, offshore Lebanon. Because the Messinian salt giant is
100 shallowly buried and only weakly deformed, it is well-imaged in seismic reflection data. Furthermore,
101 unlike older basins (e.g. offshore Brazil and Angola), the RSBs are well-preserved and not yet
102 overprinted by later tectonic deformation. They therefore provide an ideal opportunity to investigate
103 early RSB development, quantify translation along the margin, and assess implications for salt flow
104 kinematics.

105 2 Data and Methods

106 We use a large (c. 10,000 km²) 3D seismic reflection dataset located offshore Lebanon in the northern
107 Levantine Basin (Fig. 2) to investigate the stratigraphic record of RSBs and associated fluid escape
108 pipes. The dataset comprises a merge of seven time-migrated 3D seismic surveys acquired by PGS that
109 have been processed to near-zero phase with reverse SEG polarity, i.e. an increase in acoustic
110 impedance has a negative amplitude. Bin dimensions were 25 x 25 m during data processing. The
111 dominant frequencies of seismic data are 50 Hz in the overburden, 25 Hz in the Messinian evaporites,
112 and 17 Hz in the sub-salt units. The seismic resolution, calculated as a quarter of the wavelength ($\lambda/4$;
113 Brown, 2011), varies according to lithology and depth below seabed, but is estimated to be c. 10 m in
114 the clastic supra-salt overburden, c. 42 m in the Messinian salt interval and c. 44 m in the sub-salt
115 clastic strata, using average P-wave velocities of 2000 m/s, 4200 m/s, and 3000 m/s respectively
116 (Gardosh and Druckman, 2006; Reiche et al., 2014; Feng and Reshef, 2016). The seismic data image
117 down to 4000 ms two-way-time (TWT), and where thicknesses and depths are measured and quoted
118 in ms TWT, we use the average interval velocities to estimate the equivalent thickness in metres.

119 Key reflections include base-salt, top-salt and seabed. The distribution of the salt and orientation of
120 supra-salt faults and folds give context to the salt tectonic regime and basin evolution. In order to
121 analyse the development of RSBs we map in 3D their internal stratigraphy, analyse their seismic-
122 stratigraphic relationships, and generate structure and thickness (isopach) maps. We identify eight
123 well-developed RSBs that have clearly defined onlap surfaces, and select nine overlapping intra-RSB
124 horizons (O2-O10; Fig. 3) that can be confidently mapped across the margin as discrete, continuous
125 reflections (spanning c. 100 km from NE to SW). We use the migration of intra-RSB depocentres away
126 from the anticline with increasing age to determine the direction of salt flow, by tracing the position
127 of the thickest part of the depocentre through time (Pichel et al., 2018; Pichel et al., 2019). In older,
128 more deeply buried basins, the precision of this technique may be limited by later faulting, diapirism,
129 and other tectonic processes that subsequently deform the intra-RSB isopachs. However, the original
130 geometries of the young RSBs on the Levant Margin are exceptionally well-preserved.

131 Given that each onlap originally formed at the RSB hinge before being buried and translated
132 basinward, the total translation is given by the horizontal distance from the first onlap to the present
133 RSB hinge (Figs. 1 and 3). This method assumes that the position of the RSB hinge has been stable
134 through time, which we believe to be a valid assumption based on the results of numerical analogue
135 models (Pichel et al. 2018). We estimate a possible error of up to 100 m associated with picking the
136 precise onlap positions in seismic data, and incorporate these uncertainties into our analysis. We
137 assume that the mapped intra-RSB horizons represent temporally equivalent surfaces across the

138 margin, which we believe to be valid based on the lack of seismic-scale unconformities in the
139 overburden and apparently continuous sediment aggradation since the Messinian. Correlating seismic
140 horizons of the same age between different RSBs allows us to compare the magnitude of translation
141 along the margin during different time intervals, identifying lateral changes in translation rate along
142 strike. For the most part we discuss relative, rather than absolute, translation rates due the absence
143 of accurate age constraints in the supra-salt strata. One key horizon is tentatively assigned an absolute
144 age of 1.8 Ma based on a calibration with Kirkham et al. (2019) and Cartwright et al. (2018), who
145 mapped this horizon northwards from boreholes in the southern Levantine Basin into their study areas
146 (Fig. 2). Should future data (i.e. from drilling) yield further meaningful age constraints within the
147 supra-salt strata, this may be used to calculate absolute translation rates. Finally, we sum the heaves
148 of salt-detached growth faults in the updip extensional domain to compare to the translation
149 estimates given by the RSBs. Fault heave measurements are taken on seismic sections perpendicular
150 to the dominant structural trend (i.e. parallel to the direction of extension). These measurements are
151 reported to two significant figures, accounting for the uncertainty inherent in the seismic resolution.

152 We also generate variance and RMS amplitude attribute maps derived from the top-salt surface to
153 identify and map fluid escape pipes (Barnes, 2016). Features related to subsurface fluid migration have
154 been interpreted following the criteria described in literature (e.g. Cartwright and Santamarina, 2015):
155 variance maps highlight fluid escape features due their internally chaotic nature in comparison to the
156 continuous reflections characterising the surrounding stratigraphy, whereas RMS amplitude maps
157 show the anomalously low-amplitude regions where the otherwise high-amplitude, top-salt reflection
158 has been disrupted by fluid escape. Individual pipes have a cylindrical geometry and many are
159 associated with palaeo-pockmarks indicative of fluid emission (see Oppo et al., 2021). We map trails
160 of pipes and analyse their relationship with the RSBs, as well as using them to determine the direction
161 of translation by tracking a single point through time.

162 3 Geological Setting

163 The seismic dataset used in this study is situated offshore Lebanon in the Levantine Basin. The Eastern
164 Mediterranean comprises the Levantine and Herodotus Basins, separated by the Eratosthenes
165 Seamount (Fig. 2). The Levantine Basin formed in response to Permo-Triassic and Jurassic rifting
166 (Nader et al., 2018), and contains up to 20 km of clastic material overlying thin continental crust (Aal
167 et al., 2000; Inati et al., 2016). The African plate collided with the Eurasian plate in the Late Cretaceous,
168 initiating active subduction along the northern boundary of the basin.
169 The complex collision geodynamics of the region led to additional phases of compression during the
170 Late Miocene-Pliocene, generating a series of folds, thrusts, and transpressional strike-slip fault

171 movements along the Levant Margin, both onshore and offshore (Hall et al., 2005; Hawie et al., 2013;
172 Ghalayini et al., 2014).

173 A thick (up to 2 km), layered evaporitic sequence was deposited across the eastern Mediterranean
174 during the Messinian Salinity Crisis (MSC) between 5.96 and 5.33 Ma (e.g. Gautier et al., 1994; Ryan,
175 2009; Roveri et al., 2014). During this time, the Mediterranean Sea was isolated from the Atlantic
176 Ocean due to the closure of the Strait of Gibraltar, causing evaporitic drawdown and extensive salt
177 precipitation. The Messinian salt in the eastern Mediterranean is lithologically heterogeneous,
178 comprising thin, clay-rich interbeds within a halite-dominated matrix that can be imaged with seismic
179 reflection data (Netzeband et al., 2006; Gvirtzman et al., 2013; Feng et al., 2016; Meilijson et al., 2019;
180 Evans and Jackson, 2020b). When the Strait of Gibraltar reopened in the Pliocene, marine Atlantic
181 waters flooded the Mediterranean and a clastic overburden (up to 1.5 km thick) was deposited above
182 the salt. Tectonically-driven tilting of the basin margins, as well as differential loading of the salt by
183 prograding clastic wedges, triggered gravity-driven deformation of the Messinian salt (Gvirtzman et
184 al., 2013; Allen et al., 2016). The salt deformation is thought to be dominantly driven by gravity gliding
185 in the northern Levantine Basin (due to tilting of the margin), whereas gravity spreading dominates in
186 the south due to sediment loading by the Nile deep-sea fan (Allen et al., 2016).

187 Due to its complex geodynamic setting, two discrete phases of salt deformation took place on the
188 Levant margin; an early syn-depositional phase and a later post-overburden phase (Netzeband et al.,
189 2006; Bertoni and Cartwright, 2007; Gvirtzman et al., 2013; Feng et al., 2017; Kartveit et al., 2018;
190 Evans and Jackson, 2020b). The early syn-depositional phase of salt flow took place during the
191 Messinian, folding the intra-salt layers in the absence of a post-salt overburden. The crests of these
192 structures were then eroded and dissolved, creating a sub-horizontal surface against which deformed
193 intra-salt reflections are truncated (Gvirtzman et al., 2017; Kirkham et al., 2020). After a period of salt
194 tectonic quiescence and deposition of a thin, pre-kinematic clastic overburden, uplift of the Levant
195 margin in the Pleistocene initiated a second phase of salt movement driven by gravity gliding. This is
196 linked to the development of kinematically-linked zones of updip extension and downdip contraction
197 (Fig. 2) (e.g. Jackson et al., 1994), with salt-detached normal faults and associated growth strata in the
198 updip extensional domain and salt-cored buckle folds in the downdip contractional domain (Allen et
199 al., 2016; Elfassi et al., 2019; Ben-Zeev and Gvirtzman, 2020). This second phase of salt flow further
200 deformed the pre-existing intra-salt structures, over-printing the earlier syn-depositional salt
201 deformation (Evans and Jackson, 2020b).

202 The present Eastern Mediterranean region remains tectonically active. The recent uplift of the Levant
203 Margin is attributed to ongoing plate convergence (Fig. 2) (Ben-Avraham, 1978; Hall et al., 2005),

204 possibly associated with transpressional activity on the N-trending Dead Sea Transform fault network
205 (Fig. 2) (Butler et al., 1998; Gomez et al., 2008). The compressional deformation front of the Cyprus
206 Arc, dominated by the Latakia Ridge, forms the northern boundary of the Levantine Basin. The
207 western extension of the Cyprus Arc forms an accretionary wedge, known as the Mediterranean Ridge,
208 which bounds the Herodotus Basin to the north and west (Fig. 2). The north African passive margin
209 forms the southern boundary to the basin, where the Nile river system is draining the African
210 continental interior and supplying large quantities of clastic material to the rapidly prograding Nile
211 Delta (Fig. 2).

212 4 Results

213 4.1 Base-Salt Relief

214 Salt flow is known to be sensitive to the geometry of the surface that it flows across (e.g. Dooley et
215 al., 2017; Pichel et al., 2019; Evans and Jackson, 2020a). Offshore Lebanon the base-salt surface dips
216 generally to the NW, but with significant rugosity on this part of the Levant Margin (Fig. 4). The depth
217 to base-salt shallows to the south of the dataset across the Saida Fault, a Mesozoic normal fault which
218 bounds an elevated Mesozoic structural element known as the Saida-Tyr Platform (Fig. 4) (Nader et
219 al., 2018; Ghalayini et al., 2018). The Latakia Ridge crosses the northwestern corner of the dataset and
220 is expressed as a large, arcuate, broadly NE-trending anticline on both the base-salt and top-salt
221 surfaces (Fig. 4 and Fig. 5b).

222 There are several, NE-trending anticlines distributed across the margin which vary from 100 ms up to
223 820 ms in height (c. 200 m up to 1.6 km respectively) (Fig. 4). In map view they are between 8 and 28
224 km long, and are typically 2-3 km wide (Fig. 4). Although the seismic data are presented in TWT, we
225 know these anticlines are real geological structures and not seismic data artefacts (i.e. velocity pull-
226 up features) as the salt is thinner (as opposed to thicker) above the anticlines crest. Above one of the
227 largest anticlines the salt thins to as little as 30 ms (c. 70 m), from an adjacent thickness of 500 ms (c.
228 1.3 km) (Fig. 3). These anticlines are thought to have developed during the Late Miocene due to the
229 NW-SE oriented regional tectonic compression associated with continental convergence. Some folds
230 are symmetrical whereas other show a steep forelimb and a gently-dipping backlimb (e.g. Fig. 3),
231 characteristic of fault-propagation folds overlying deeper thrust faults (Ghalayini et al., 2014; Ghalayini
232 et al., 2018). Several of the folds are associated with contemporaneous transpressional reactivation
233 of the Saida Fault (Fig. 4) (Ghalayini et al., 2014). They therefore predate deposition of the Messinian
234 salt, although it is possible that there may have been some later amplification of these structures in
235 response to ongoing compression (Hawie et al., 2013; Ghalayini et al. 2014).

236 We also note the base-salt is offset by evenly-spaced, NW-SE striking, short (up to 6 km), low-
237 displacement (30-60 ms throw; c. 50-90 m) normal faults that are particularly common in the deeper
238 basin (Fig. 4). In cross section these appear to be layer-bound, sub-salt normal faults terminating at
239 the base-salt, and that do not extend upwards into the overlying salt. These have been interpreted as
240 Late Miocene syn-sedimentary faults that formed in response to an anisotropic stress field (Ghalayini
241 et al. 2017; Reiche et al., 2014).

242 4.2 Salt Distribution and Supra-Salt Structure

243 The Messinian salt layer overall thickens westward into the deep Levantine Basin and thins updip,
244 pinching out onto the Levant Margin (Fig. 5a). The evaporite sequence is lithologically heterogeneous,
245 leading to internal seismic reflectivity within the deforming salt sheet (e.g. Fig. 6) (Netzeband et al.,
246 2006; Gvirtzman et al., 2013; Feng et al., 2016; Meilijson et al., 2019; Evans and Jackson, 2020b). The
247 intrasalt reflections are folded and faulted, and are truncated landward against the top-salt due to an
248 earlier, syn-depositional phase of deformation, erosion, and dissolution (Gvirtzman et al., 2013;
249 Gvirtzman et al., 2017; Feng et al., 2017; Kartveit et al., 2018; Kirkham et al., 2020; Evans and Jackson,
250 2020b).

251 The supra-salt structure of the basin can be divided into kinematically-linked domains of updip
252 extension and downdip contraction, separated by a relatively undeformed translational domain (Fig.
253 2). The present dataset mostly covers the extensional and upper translational domains, with minimal
254 contraction in the overburden, except where the Latakia Ridge locally restricts salt flow in the north,
255 resulting in the formation of NE-trending buckle folds (Fig. 5b) (Allen et al., 2016; Evans and Jackson,
256 2020b). The extensional domain is dominated by salt-detached normal faults and associated salt
257 rollers that strike sub-parallel to the margin, perpendicular to the base-salt dip (Fig. 5b and 6). A small
258 region towards the north of the dataset is dominated by local reactive diapirism (Fig. 5b). The trend
259 of these structures is consistent with a dominant NW direction of translation driven by gravity gliding
260 (Evans and Jackson, 2020b). The dominant strike of the supra-salt faults rotates toward the south,
261 from NNE to ENE, closely following the geometry of the base-salt surface and orientation of the salt
262 pinch-out (Fig. 5b). Several faults in the far south of the dataset trend NW, perpendicular to the margin
263 and parallel to a base-salt high (Fig. 4a), and do not accommodate basinward salt-detached
264 translation.

265 4.3 Ramp Syncline Basins (RSBs)

266 The NE-trending sub-salt anticlines are associated with supra-salt RSBs positioned above and adjacent
267 to their basinward flanks, recording the progressive basinward translation of the salt and overburden

268 over the anticlines. They can be easily recognised in cross section by their characteristic landward-
269 dipping, asymmetric growth strata (Fig. 3). The growth strata packages thicken toward, and terminate
270 against, the basal RSB 'onlap surface'. The onlap surface is diachronous, cutting up through the
271 stratigraphy and younging toward the anticline. The surface typically has a listric geometry in cross
272 section, being steepest at the youngest stratigraphic level and flattening with depth and distance from
273 the anticline (Fig. 3). The listric geometry causes the onlapping intra-RSB horizons to rotate downward
274 as they are translated away from the anticline, thus forming pseudo-downlaps (Fig. 3). The thickness
275 of sediment beneath the RSB (i.e. between the onlap surface and the top-salt) also increases toward
276 the anticline, reflecting the amount of sediment accumulated updip prior to translation into the RSB
277 depocentre. These observations are all consistent with RSB geometries described by previous authors
278 and generated by numerical models of overburden translation over base-salt steps (Pichel et al.,
279 2018).

280 Two of the RSBs are situated adjacent to one another, above two parallel base-salt anticlines with an
281 across-strike spacing of only c. 10 km (Fig. 7). The dual development of the two RSBs means that strata
282 in the basinward RSB onlap strata in the landward RSB, such that the two basins may become vertically
283 juxtaposed with continued translation (forming stacked RSBs; see Pichel et al., 2018).

284 Small base-salt anticlines (c. 100 ms) are associated with poorly-developed RSBs whose onlap surface
285 is difficult to trace, and that show only very subtle landward expansion of growth strata. This is
286 attributed to the small amplitude of the anticline relative to the total salt thickness, which means that
287 the associated depocentre is relatively small (Pichel et al., 2018). We also observe partially-formed
288 RSBs within the extensional domain, disrupted by normal faults (Fig. 8). These represent a kinematic
289 system whereby basinward translation of undeformed overburden is intermittently interrupted by slip
290 on normal faults, causing RSB development to 'switch on and off' (Fig. 8). This observation shows that
291 RSB development is not limited to the translational domain, as suggested by previous studies, but can
292 occur anywhere on the margin where salt translates over base-salt relief. However, RSBs developing
293 in extensional settings are more likely to be disrupted by normal faulting and associated salt structures
294 (e.g. reactive diapirs, pillows). Such structures preferentially nucleate over the crest of the anticlines
295 where there is a salt flux imbalance (Dooley et al., 2017), thus disrupting the continuous basinward
296 translation that is required to maintain the RSB.

297 Eight RSBs are well-developed and have a clearly defined onlap surface, thus providing a reliable
298 record of continuous basinward translation (Fig. 9e). Onlaps can be observed adjacent to the anticlines
299 at the present-day sea floor, where the RSB 'hinge' is typically represented by a bathymetric low,
300 indicating ongoing RSB development and basinward translation (e.g. Fig. 3). The onlap surface does

301 not, however, reach down to the top-salt, instead terminating against a thin (average 170 m or c. 170
302 m), largely isopachous (but overall basinward-thinning) supra-salt unit. This represents the pre-
303 kinematic layer (deposited prior to initiation of RSB development). The oldest intra-RSB strata
304 therefore directly onlap onto this pre-kinematic unit (e.g. Fig. 3).

305 The intra-RSB units show elongate depocentres sub-parallel to the origin anticlines with maximum
306 thickness in the centre of the RSB (Fig. 9a). Similarly, onlap surfaces show the greatest depression in
307 the centre of the RSB, adjacent to the maximum height of the anticline (Fig. 9b). The migration of
308 intra-RSB depocentres indicate a linear NW direction of translation (Fig. 9c). The present-day RSB
309 hinges and the intra-RSB onlaps have a linear or curvilinear expression in map-view, trending parallel
310 or sub-parallel to the anticline from which they originate (Fig. 9d). The length of the onlaps (and of the
311 corresponding RSB depocentre) is equal to the length of the adjacent anticline (Fig. 9e).

312 4.4 Fluid Escape Pipes

313 Several of the RSBs are cross-cut by vertical features that have an internally chaotic or transparent
314 seismic expression (Figs 3, 6 and 7). They extend vertically between the top-salt and the diachronous
315 RSB onlap surface, commonly being capped by a pockmark. In map view they form linear trails and are
316 interpreted as trails of fluid escape pipes (Fig. 10) (Cartwright et al., 2018; Kirkham et al., 2019; Oppo
317 et al., 2021). As well as the vertical pipes preserved within the overburden, in some places we can also
318 identify the arcuate traces of the deformed pipes preserved within the salt sheet itself, connecting the
319 base of the pipe at the top-salt to its origin in the sub-salt anticline (Fig. 7). The pipes invariably root
320 to the crest or the downdip flank of the anticlines, indicating a sub-salt origin for the escaped fluids,
321 with the anticlines acting as traps and the salt as an imperfect seal (Al-Balushi et al., 2016; Cartwright
322 et al., 2018; Oppo et al., 2021).

323 We identify twelve pipe trails in the dataset, all of which originate from sub-salt anticlines that also
324 generate RSBs (Fig. 9e). After vertical emission above the anticline, the pipes are translated into the
325 RSB depocentre where they become buried, and the pockmark is onlapped by the RSB growth strata
326 (Fig. 1). Critically, this means that the age of each pipe is approximately equivalent to the age of the
327 horizon that meets the pockmark at the onlap surface (Fig. 1). This allows us to constrain the relative
328 ages of pipes in different trails and different, widely-spaced RSBs (Fig. 9d). This reveals that the oldest
329 pipes in each trail are not the same age, though the oldest pipe in several trails appears close to the
330 oldest RSB onlap (e.g. Fig. 9d).

331 Some trails form a well-defined linear trend, whereas others show significantly more scatter,
332 indicating that the precise emission point may vary slightly through time (Fig. 9d). They can be treated
333 as direct kinematic vectors of transport direction at different localities along the margin (Fig. 9d). All

334 pipe trails identified in the present study trend broadly NW, indicating a NW direction of translation,
335 which is consistent with the direction indicated by the migration of RSB depocentres and the
336 orientation of supra-salt faults updip. They do, however, show some variation in the precise direction
337 of translation along margin, rotating from a more WNW bearing in the northern part of the dataset
338 (295°) to a more NNW bearing in the south (335°). This rotation in transport direction is consistent
339 with the observed change in the strike of faults in the updip extensional domain (Evans and Jackson,
340 2020b).

341 The deformed pipes provide a unique means to examine the internal flow dynamics of a deforming
342 salt sheet, whereas in the past much of our understanding has had to rely on numerical and physical
343 analogue models, with few ways of constraining the natural systems themselves (e.g. Davison et al.,
344 1996; Albertz and Ings, 2012). We observe arcuate pipe geometries that flatten with depth and are
345 largely consistent with those of the previous studies (Cartwright et al., 2018; Kirkham et al., 2019),
346 where the authors use the inclined nature of the deformed pipes to infer a dominant Couette (i.e.
347 drag-induced) flow profile within the salt sheet.

348 4.5 Kinematic Analysis

349 Integrating the information given by the RSBs and fluid escape pipes, we can analyse lateral variations
350 in the magnitude and direction of translation recorded at different localities along the northern
351 Levantine Basin margin. The intra-RSB onlaps give the magnitude of translation and some indication
352 of the direction, but since their orientation is most sensitive to the orientation of the anticline from
353 which they originate, they may be oblique to the actual direction of translation shown by the pipes
354 (e.g. RSB 8 in Fig. 9e). The translation direction is therefore more precisely constrained by the
355 orientation of the pipe trails or the migration direction of the RSB depocentres (Fig. 9c-d).

356 The first onlap onto the pre-kinematic layer at the base of the RSB records the initiation of RSB
357 development, and therefore the onset of salt-detached gravity gliding of the overburden (O10 in Fig.
358 3). Note that this constitutes the second main phase of salt deformation on the Levant Margin, with
359 an earlier phase of syn-depositional deformation occurring prior to overburden deposition (Gvirtzman
360 et al., 2013; Gvirtzman et al., 2017; Feng et al., 2017; Kartveit et al., 2018; Kirkham et al., 2020; Evans
361 and Jackson, 2020b). The age of this first onlap (O10) appears to be the same (or within two
362 reflections) for all RSBs mapped in this study, meaning that the onset of gravity gliding was broadly
363 synchronous across the margin. This horizon also appears to correspond to the 1.8 Ma age horizon
364 indicated by Kirkham et al. (2019) (based on a correlation with well data from the southern Levantine
365 Basin, offshore Israel).

366 The total amount of translation for each RSB varies between c. 5 and 7 km (Onlap 10 in Fig. 11a). This
367 represents a scatter of up to 17% about the mean of c. 6.0 km (± 100 m), with an average absolute
368 deviation of c. 0.6 km (± 100 m). This variability in translation magnitude equates to variability in the
369 average rate of overburden translation along the margin; from c. 2.8 up to 3.9 mm/yr (± 0.1 mm/yr),
370 assuming that the 1.8 Ma horizon represents the onset of gravity gliding. RSB 6 has the largest
371 magnitude of translation (c. 7.0 km ± 100 m) and is located 60 km from RSB 2, which has the smallest
372 magnitude of translation (c. 5.0 km ± 100 m). RSBs 1-3 in the north of the study area have overall
373 shorter translation magnitudes than RSBs 4-8, indicating overall slower average translation rates for
374 the northern segment of the margin (Onlap 10 in Fig. 11a). RSBs 4-8 do not show any systematic spatial
375 trend from north to south along the margin (i.e. increasing or decreasing magnitudes of translation
376 from north to south). We do not identify any discrete strike-slip faults accommodating the differential
377 translation rates within the overburden. This means that the rigid overburden has accommodated a
378 very modest shear strain of c. 0.03 (2 km/60 km), with an angular shear of 2°, between RSBs 6 and 2.

379 The basinward translation of RSBs is accommodated updip by extension of the overburden; reactive
380 diapirs for RSBs 1-3, and a network of salt-detached normal faults for RSBs 4-8 (Fig. 5b and Fig. 6).
381 Summing the horizontal components of slip (i.e. heave) of faults in the extensional domain gives a
382 horizontal translation estimate that we can compare to the RSB-derived estimates of total translation
383 (Fig. 12). This method yields extension values of c. 4.7-7.0 km, which are largely consistent with
384 translation estimates from the RSBs (Fig. 12). Profile 1 sums to c. 7.0 km of horizontal displacement,
385 which is consistent with the c. 7.0 km (± 100 m) of translation recorded by RSB 6 downdip. Profiles 3,
386 4 and 5 give c. 6.1-6.6 km of horizontal displacement, which is consistent with the c. 6.7 and 6.3 km (\pm
387 100 m) of translation recorded by RSB 4 and RSB 5, respectively. Conversely, the horizontal
388 displacement estimate derived from Profile 2 (c. 5.5 km) is significantly less than that recorded by RSB
389 6 downdip (c. 7.0 km ± 100 m), likely due to missing strain accommodated by sub-seismic faults. Note
390 that we cannot compare fault heaves updip of RSBs 1, 2 or 3 given this domain is dominated by
391 reactive diapirism, or for RSBs 7 and 8, due to the updip domain laying outside of the southern limit
392 of the dataset (Fig. 12). Overall, translation estimates from fault heaves support the apparent lateral
393 variability in translation rates along the margin derived from the RSBs (Fig. 12).

394 As well as total translation estimates, we can compare the translation magnitudes for other intra-RSB
395 horizons of equivalent ages (Fig. 11a), and use these to calculate the incremental translation during
396 different time intervals (Fig. 11b). For example, the distance between Onlap 10 and Onlap 9 gives the
397 distance that each RSB moved during that interval of time (Fig. 11b). We can therefore use this to
398 compare the relative translation rates of the RSBs through time. These incremental translations show
399 significantly more variability between different RSBs than the total translations, with some time

400 intervals showing a scatter of up to 80% about their average (e.g. O6-O5 gives values within the range
401 c. 100-900 m (± 100 m) with an average of c. 500 m ± 100 m) (Fig. 11b). Furthermore, we see that the
402 relative velocity of each RSB varies through time (i.e. the fastest and slowest RSBs on average, RSB 6
403 and RSB 2 respectively, have not been consistently fastest or slowest through time) (Fig. 11b). For
404 example, the incremental translations show that the relatively large magnitude of translation
405 recorded by RSB 8 is primarily due to a very recent episode of increased velocity that was not
406 experienced by the other RSBs (O2-Hinge in Fig. 11b). In fact, all RSBs appear to experience 'pulses' of
407 faster translation rates punctuated by periods of slower translation rates, such that the seemingly
408 random variability observed on short (c. 100-200 Kyr) timescales averages out over longer (c. 1-2 Myr)
409 timescales. After one RSB experiences a faster 'pulse', it then slows relative to the others, such that
410 all RSBs 'keep-up' with each other to a certain degree over long enough timescales. This means that
411 the average translation rate would eventually converge to a common value for all RSBs along the
412 margin given a long enough time period.

413 5 Discussion

414 The young and active RSBs offshore Lebanon provide an excellent stratigraphic record of the
415 magnitude and timing of salt-detached gravity gliding. As the rigid overburden slides on the ductile
416 salt layer, the RSB depocentres and onlapping strata are progressively transported downdip from the
417 adjacent causal anticline, allowing us to quantify the incremental basinward translation through time.
418 The direction of translation is constrained by tracing the RSB depocentres through time, or by using
419 the orientation of fluid escape pipe trails, which track a single point through time and thus give a direct
420 kinematic vector.

421 The temporal correlation of the oldest onlap surface between the RSBs suggests that they developed
422 at approximately the same time, and therefore that the onset of gravity gliding was broadly
423 synchronous across the entire margin (c. 1.8 Ma). This roughly coincides with the age of the oldest
424 fluid escape pipes in the region (though not all pipe trails initiated at this time; see Oppo et al., 2021).
425 Therefore, the initiation of gravity gliding and fluid escape is broadly contemporaneous across the
426 entire northern Levantine Basin, suggesting a single trigger for both events. The most recent phase of
427 uplift of the Levantine margin was recorded by a change in drainage direction in northern Israel
428 starting at c. 1.8 Ma (Matmon et al., 1999), thought to be related to ongoing convergence between
429 the African and Eurasian plates. This uplift could have increased the tilt of the base-salt enough to
430 generate gravitational instability and initiate post-Messinian gravity gliding. At the same time, the
431 basin tilt would have also favoured updip fluid (e.g. oil and gas) migration from the deep basin towards

432 the anticlines along the basin margin (Oppo et al., 2021). The updip fluid migration filling the sub-salt
433 traps, as well as possible exsolution of gas from oil due to a decrease in pressure, could have led to
434 supra-lithostatic overpressure within the anticlines, thus triggering cross-evaporite fluid escape (Oppo
435 et al., 2021).

436 The original study to identify a pipe trail associated with an anticline in the deep Levantine Basin
437 (termed the Oceanus structure) used the horizontal distance from the oldest pipe to the present
438 emission point to estimate the magnitude of translation (3.4 km) (Cartwright et al., 2018). Assuming
439 this to be the total translation since deposition of the 1.8 Ma marker horizon, the authors calculate an
440 average translation rate of 2.0 mm/yr. However, the RSB onlaps show that translation actually
441 initiated prior to the emission of the first pipe, and that the distance from the first onlap onto the 1.8
442 Ma horizon to the present RSB hinge in fact suggests 4.6 km of translation in this time (see Fig. 2b in
443 Cartwright et al., 2018). This yields a faster translation rate of c. 2.7 mm/yr (± 0.1 mm/yr) (i.e. 35%
444 higher than that estimated from the pipes alone). The RSB onlaps also show that the overburden has
445 thickened through time, from a thin (c. 120 m) pre-kinematic layer at 1.8 Ma to the present thickness
446 (c. 400 m). This means that the stress acting on the salt has increased through time and it is therefore
447 more accurate to use a time-averaged overburden thickness than present-day overburden thickness
448 when calculating viscosity (ratio of shear stress to shear strain rate; see supplementary info in
449 Cartwright et al., 2018). However, the recalculated viscosity (1.1×10^{18} Pa s) using the newly
450 constrained translation rate (c. 2.7 mm/yr) and time-averaged overburden thickness (c. 260 m
451 assuming constant sedimentation rate) is of the same order of magnitude as that estimated by the
452 previous study (2.3×10^{18} Pa s; Cartwright et al., 2018). Both values fall within the expected viscosity
453 range derived from other natural examples and from laboratory experiments of rock salt rheology
454 ($10^{17} - 10^{20}$ Pa s) (Urai and Spiers, 2007; Urai et al., 2008; Mukherjee et al., 2010).

455 Another previous study investigated four closely spaced pipe trails within RSB 8, associated with the
456 southernmost anticline in the present dataset (Saida-Tyr structure; Fig. 4) (Kirkham et al., 2019). The
457 authors postulate the presence of 'streams' of fast-flowing salt based on the assumption that the first
458 pipe in each trail formed at the same time (Fig. 13). However, using the intra-RSB onlaps to constrain
459 the relative ages of the first pipes, which are not in fact the same age, we show that c. 1.5 km of
460 translation had actually occurred between the formation of the oldest pipe in trail STP 1 and the oldest
461 pipe in trail STP 3 (Fig. 13). This observation does not support large across-strike differences in salt
462 flow velocity across a single RSB and questions the presence of fast-flowing salt streams. In fact, the
463 sub-parallel intra-RSB onlaps mapped show that local rates of basinward translation are approximately
464 uniform over individual km-scale anticlines (i.e. we do not see any major rotation or deformation of
465 onlaps as they are translated away from the anticline; Fig. 13). However, our correlation of horizons

466 between different RSBs along the margin shows that both the direction and rate of translation *do* vary
467 significantly through space and time over a larger spatial scale. This leads us to discuss two possible
468 mechanisms that may be controlling this lateral variability in translation rate along the margin.

469 5.1 Salt Flux Imbalance and Cyclical 'Pulses' of Flow

470 Thinning of the salt over the crests of the anticlines leads to an imbalance in salt flux. On the updip
471 flank of the anticlines there is a large volume of salt forced to squeeze through a relatively small gap
472 between the sub-salt anticline and relatively strong clastic overburden. Physical analogue models
473 show that salt flux imbalances such as this can cause temporal variations in salt (and overburden)
474 velocity (Dooley et al., 2017). A simple experiment modelling salt flow up onto a base-salt high shows
475 that during the early stages of deformation, the salt slows down and inflates as flow lines converge
476 (see Fig. 18 in Dooley et al., 2017). Subsequently, as the salt above the high thickens, the effects of
477 basal drag are minimised and the salt accelerates. Some anticlines in the present study show evidence
478 of inflation on the updip flank of subsalt anticlines (e.g. Fig. 3), and we therefore propose a similar
479 mechanism may play a role in modulating local rates of salt and overburden translation here (Fig. 14).

480 In the first instance, pressure builds within the salt on the updip flank due to the volumetric mismatch
481 (more salt input than output) (Fig. 14a). This may also be associated with inflation, though the
482 confining pressure from the overburden weight resists this. On the downdip flank the flux imbalance
483 causes the salt to thin and overburden to subside (more salt output than input), creating the RSB
484 depocentre adjacent to the anticline (Fig. 1). This process gradually increases the pressure difference
485 (ΔP) across the anticline (Fig 14a T0-T1). In turn, this pressure difference increases the stress acting
486 upon the salt, and since stress is proportional to strain rate, the velocity of salt flow across the anticline
487 increases (Fig 14a, T0-T1). The premise that stress is proportional to strain rate applies to Newtonian
488 fluids, which is a valid approximation in this case where the stress is relatively low and pressure
489 solution is the dominant mechanism of salt flow (Spiers et al., 1990; Van Kekan et al., 1993; Urai et al.,
490 2008). The acceleration of the salt is proportional to the pressure difference across the anticline, such
491 that maximum acceleration occurs when ΔP is at its peak (Fig. 14a, T1). This velocity increase reduces
492 the volumetric imbalance across the anticline and allows the pressure difference to drop (Fig. 14a, T1-
493 T2). As the system approaches equilibrium, the stress acting on the salt is reduced and it begins to
494 decelerate (Fig. 14a, T2-T3). The pressure difference across the anticline then starts to build up again,
495 and the process repeats (Fig 14a, T3-T4). This mechanism would allow for cyclical 'pulses' of faster salt
496 flow (and overburden translation) during certain time intervals. The timing of the salt 'pulses' would
497 vary for different anticlines depending on the thickness of the salt over the anticline, the adjacent salt
498 thickness updip, and the thickness of the overburden, amongst other variables. There may also be a

499 component of out-of-plane salt flow not included in this simplified model, but there is no evidence of
500 this in the supra-salt structure and it is therefore thought to be relatively minor.

501 The anticlines associated with the RSBs in this study have maximum heights between c. 220-820 ms
502 (c. 430 m up to 1.6 km). The thickness of salt over the anticlines tends to be inversely proportional to
503 their height, with larger anticlines generally capped by thinner salt over their crests (though not all
504 anticlines adhere to this trend) (Fig. 15a). The difference between the adjacent thickness of salt updip,
505 and the thickness of salt over the crest, can be used as a proxy for salt flux imbalance (Fig. 15a). This
506 means that we would expect anticlines with a large thickness of adjacent salt and very thin salt over
507 their crest to have a large salt flux imbalance. Some anticlines are therefore associated with larger salt
508 flux imbalances than others (Fig. 15a).

509 This observation and inference could explain why some RSBs demonstrate more extreme 'pulses' of
510 salt flow than others (Fig. 11b). In order to evaluate this variability quantitatively, we calculate the
511 average absolute deviation for each RSB. The absolute deviation is the difference between the
512 translation distance recorded by the RSB at a given time interval, and the average translation distance
513 for that time interval (Fig. 11b). These absolute deviations are then averaged across all time intervals
514 for each RSB. We find that the average absolute deviation is proportional to the salt flux imbalance
515 with an R^2 value of 0.9 (Fig. 15b). This means that RSBs with a greater salt flux imbalance deviate more
516 widely from the average magnitude of translation at each time step, and thus the more extreme its
517 fluctuations in translation rate (Fig. 15b). We suggest that this is because where the volumetric
518 imbalance is relatively small (i.e. salt thickness is more uniform across the anticline), pressure
519 differences are released more easily (Fig. 14b). Consequently, the 'pulses' of faster and slower
520 translation are less extreme, and translation rates are generally more consistent over time (Fig. 14b).
521 This is the case for RSBs 4 and 5 (Fig. 15b). Conversely, the anticlines with the greatest flux imbalance
522 show more extreme variability because they must build up a greater pressure difference in order to
523 equilibrate over the anticline (Fig. 14a). This is the case for RSBs 2, 3 and 8 (Fig. 15b). We note that
524 there may have been some post-Messinian amplification of these anticlines absorbed by salt thinning,
525 which would further augment the salt flux imbalance over time, but the lack of stratigraphic evidence
526 for overburden uplift suggests that this would have been relatively minor.

527 This mechanism could also explain why even the dual RSBs (2 and 3) show slightly different rates of
528 translation (Fig. 11). The anticlines associated with RSB 2 and RSB 3 are 10 km apart and parallel to
529 one another (Fig. 7 and Fig. 9e). They record translation on the same part of the margin, but show
530 slightly different magnitudes of total translation. It appears that the landward RSB has translated
531 further than the basinward RSB (5.3 km and 4.9 km respectively), as well as experiencing slightly

532 different magnitudes of incremental translation through time (Fig. 11b). The anticlinal geometry of
533 the landward intra-RSB strata could suggest that the additional 400 m of translation may have been
534 accommodated via shortening in the form of large-scale folding, as well as possible cryptic lateral
535 compaction (Fig. 7) (e.g. Butler and Paton, 2010).

536 While salt flux imbalances may play a key role in modulating local rates of translation over individual
537 base-salt anticlines, there is another key control that we also need to consider. The Couette flow
538 profile inferred from the geometry of the deformed pipes indicates that drag on the top-salt surface
539 is the dominant driver of salt deformation in this area (Cartwright et al., 2017; Kirkham et al., 2019).
540 This means that it is the translation of the overburden that is driving salt deformation. We must
541 therefore consider mechanisms that facilitate the basinward translation of the overburden, in order
542 to fully understand the differential rates of overburden translation and how the RSBs interact with
543 one another.

544 5.2 Overburden Mechanics and Elastic Strain

545 An additional mechanism that could be controlling translation rates of the salt and its overburden is
546 the distribution of elastic stress and strain in the relatively rigid overburden. If we treat the overburden
547 as a uniform sheet (Fig. 16a) and apply a tilt (Fig. 16b), the gravitational force acting on the tilted
548 overburden, and therefore the tectonic stress, is approximately constant along the margin but
549 increases updip (where the weight of the downdip sheet is greatest). This causes elastic strain to build
550 up within the overburden, which is proportional to the applied stress and therefore also increases
551 updip (Fig. 16b). When the stress exceeds the strength of the overburden, brittle failure occurs and
552 faults develop (Fig. 16c-f). The development and growth of these faults thus facilitates the basinward
553 translation of the overburden (Fig. 6). If the faults eventually evolve into reactive diapirs, as is the case
554 for RSBs 1-3, it is then the widening of the diapirs that facilitates the basinward translation.

555 However, the extent to which these faults control the rate of translation in the translational domain
556 downdip depends largely on whether the mechanical behaviour of the overburden is dominantly
557 plastic or dominantly elastic. In a dominantly plastic deformation model, where materials deform at
558 constant stress, the translational domain is permitted to pull away at a uniform rate, with faults updip
559 locally releasing the elastic strain when brittle failure (i.e. fault slip) occurs (Fig 16c,e). In a dominantly
560 elastic deformation model, where strain is directly proportional to stress, the tension in the sheet is
561 maintained and the faults updip allow the sheet downdip to pull forward by a magnitude dictated by
562 the fault heave (Fig. 16d,f). In reality, the mechanical behaviour of the overburden at the margin scale
563 is elasto-plastic (Weijermars et al., 1993) and therefore the actual overburden deformation is a hybrid
564 of these two end-member models. In either case, this means that the rate of basinward translation in

565 the extensional and upper translational domains, where the majority of RSBs are located, is
566 intrinsically linked to the slip rate on the faults (Fig. 16). These faults move at different times, due to
567 a number of independent variables in the system (rheological heterogeneity, geometry of the fault
568 plane, pore fluid pressure, etc.) that make it very difficult to predict when or in which order the
569 different fault segments will slip. This phenomenon is well-documented on fault networks in areas of
570 active extension, with many studies showing that fault activity is inherently episodic and that slip rates
571 vary through time and space (e.g. Mitchell et al. 2001; Benedetti et al. 2002; Friedrich et al. 2003; Bull
572 et al. 2006; Nicol et al. 2006; McClymont et al. 2009; Schlagenhauf et al. 2010, 2011; Cowie et al.,
573 2012). This may explain some of the seemingly random variability in rates of translation along the
574 margin. Note that this simplified model considers only the mechanics of the updip extensional and
575 translational domains, and further complexity may be introduced by incorporating stresses within the
576 contractional domain downdip. Nevertheless, this gives valuable insights into some key controls in the
577 updip region where the RSBs are situated.

578 Furthermore, these faults transfer elastic strain and stress between different segments of the
579 overburden during each slip event (e.g. Cowie 1998; Robinson et al. 2009; Cowie et al., 2012). If one
580 part of the relatively rigid overburden sheet is moving faster than the adjacent segment, as the RSBs
581 have shown, this difference would have to be accommodated by a discrete NW-trending strike-slip
582 fault, or distributed over a wider zone and stored as shear strain. Strike-slip faults are observed in the
583 overburden offshore Israel where they offset subaqueous channels (Cartwright et al., 2012; Clark and
584 Cartwright, 2009; Kartveit et al., 2018), and likely accommodate differential rates of salt-detached
585 translation between different segments of the margin. However, we do not identify similar salt-
586 detached strike-slip faults in the overburden offshore Lebanon, and therefore infer that the
587 differential translation must be accommodated by distributed elastic shear strain. Since the
588 overburden is a relatively rigid sheet, it can only accommodate a certain amount of elastic strain
589 without brittle failure. This means that when one fault ruptures and a segment moves locally, this
590 increases the elastic strain in neighbouring segments, thus bringing them closer to failure (Fig. 16c-d).
591 This strain is then released when the neighbouring segments slip and 'catch up' with the first segment
592 (Fig. 16e-f). We therefore envisage that the distribution of stress and storage of elastic strain in the
593 overburden could explain the fact that all segments appear to 'keep-up' with each other over long
594 timescales. Although we have illustrated the role of faults here, this model applies equally to RSBs 1-
595 3, whose translation is presently accommodated by reactive diapirs, as long as the overburden
596 remains unbroken by strike-slip faults. Essentially, this demonstrates that over margin-scale lengths
597 the overburden undergoes a process of tectonic 'stretching and squeezing' as it translates basinward,
598 rather than uniformly translating as a perfectly rigid material. Because the overburden in the

599 Levantine Basin is relatively young and shallowly buried, it may be able to accommodate more elastic
600 strain than thicker, more compacted and consolidated clastic overburdens in other basins (Butler and
601 Paton, 2010; Burberry, 2015).

602 We conclude that the interplay between the cyclical 'pulsing' of salt flow over base-salt anticlines and
603 the mechanical behaviour of the overburden dominantly control differential rates of basinward
604 translation on the Levant Margin. While the cyclical flux of salt over the anticlines controls variability
605 on shorter timescales (on the order of 100 Kyr), the distribution of elastic strain in the overburden will
606 ensure that all segments of the margin keep up with each other on longer timescales (on the order of
607 1 Myr). These two processes will be superimposed to create the observed variability in translation
608 rates along the margin. Similar processes are expected to operate in other salt basins undergoing
609 gravity-driven deformation.

610 6 Conclusions

- 611 • The well-developed ramp syncline basins offshore Lebanon are excellent records of
612 translation on a salt-influenced passive margin dominated by gravity-gliding
- 613 • Pipe trails provide direct vectors of transport direction, and the relative ages of the pipes can
614 be determined by correlating intra-RSB horizons across the margin
- 615 • Rates of basinward translation are approximately uniform at the km-scale but show significant
616 lateral variability at the margin-scale
- 617 • Differential translation rates may be a result of pulsed salt flow due to volumetric imbalance
618 over the base-salt anticlines
- 619 • The overburden deforms as it translates, with the distribution of stress and elastic strain
620 ensuring that differential translation rates average out over long timescales

621 Acknowledgements

622 The authors would like to thank Tim Dooley, Frank Peel and other members of the Applied
623 Geodynamics Laboratory at UT Austin for valuable discussions that helped to shape our
624 interpretations. We also thank Jessica Thompson Jobe and an anonymous reviewer for constructive
625 feedback that strengthened the manuscript. We gratefully acknowledge Ramadan Ghalayini, Wissam
626 Chbat and the Lebanese Petroleum Administration for the provision of data without which this project
627 would not have been possible. Data supporting this research are available for academic purposes at
628 the discretion of the Lebanese Petroleum Administration, under confidentiality agreements, and are
629 not currently accessible to the public. Up-to-date contact details may be found at [www.lpa.gov.lb].
630 Seismic interpretation was facilitated by Schlumberger's Petrel software, provided on an academic
631 license.

632 References

- 633 Aal, A.A., El Barkooky, A., Gerrits, M., Meyer, H., Schwander, M. and Zaki, H., 2000. Tectonic evolution
634 of the Eastern Mediterranean Basin and its significance for hydrocarbon prospectivity in the
635 ultradeepwater of the Nile Delta. *The Leading Edge*, 19(10), pp.1086-1102.
- 636 Al-Balushi, A.N., Neumaier, M., Fraser, A.J. and Jackson, C.A., 2016. The impact of the Messinian
637 salinity crisis on the petroleum system of the Eastern Mediterranean: a critical assessment using 2D
638 petroleum system modelling. *Petroleum Geoscience*, 22(4), pp.357-379.
- 639 Albertz, M. and Ings, S.J., 2012. Some consequences of mechanical stratification in basin-scale
640 numerical models of passive-margin salt tectonics. *Geological Society, London, Special Publications*,
641 363(1), pp.303-330.
- 642 Allen, H., C.A.-L. Jackson and A.J. Fraser, 2016, Gravity-driven deformation of a youthful saline giant:
643 the interplay between gliding and spreading in the Messinian basins of the Eastern Mediterranean:
644 *Petroleum Geoscience*, v. 22, p. 340-356.
- 645 Barnes, A., 2016. *Handbook of Poststack Seismic Attributes*. Society of Exploration Geophysicists.
- 646 Ben-Avraham, Z., 1978. The structure and tectonic setting of the Levant continental margin, eastern
647 Mediterranean. *Tectonophysics*, 46(3-4), pp.313-331.
- 648 Ben Zeev, Y. and Gvirtzman, Z., 2020. When Two Salt Tectonics Systems Meet: Gliding Downslope the
649 Levant Margin and Salt Out-Squeezing From Under the Nile Delta. *Tectonics*, 39(12),
650 p.e2019TC005715.
- 651 Benedetti, L., Finkel, R., Papanastassiou, D., King, G., Armijo, R., Ryerson, F., Farber, D. & Flerit, F.,
652 2002. Post-glacial slip history of the Sparta fault (Greece) determined by ³⁶Cl cosmogenic dating:
653 evidence for non-periodic earthquakes, *Geophys. Res. Lett.*, 29, 1246, doi:10.1029/2001GL014510.
- 654 Bertoni, C. and Cartwright, J.A., 2007. Major erosion at the end of the Messinian Salinity Crisis:
655 evidence from the Levant Basin, Eastern Mediterranean. *Basin Research*, 19(1), pp.1-18.
- 656 Brown, A.R., 2011. *Interpretation of three-dimensional seismic data*. Society of Exploration
657 Geophysicists and American Association of Petroleum Geologists.
- 658 Brun, J.P. and Fort, X., 2011. Salt tectonics at passive margins: Geology versus models. *Marine and
659 Petroleum Geology*, 28(6), pp.1123-1145.
- 660 Bull, J.M., Barnes, P.M., Lamarche, G., Sanderson, D.J. Cowie, P.A., Taylor S.K. & Dix, J.K., 2006. High-
661 resolution record of displacement accumulation on an active normal fault: implications for models of
662 slip accumulation during repeated earthquakes, *J. Struct. Geol.*, 28, 1146–1166.
- 663 Burberry, C.M., 2015. Spatial and temporal variation in penetrative strain during compression: Insights
664 from analog models. *Lithosphere*, 7(6), pp.611-624.
- 665 Butler, R.W.H. and Paton, D.A., 2010. Evaluating lateral compaction in deepwater fold and thrust belts:
666 How much are we missing from “nature’s sandbox”. *GSA Today*, 20(3), pp.4-10.
- 667 Butler, R.W.H., Spencer, S. and Griffiths, H.M., 1998. The structural response to evolving plate
668 kinematics during transpression: evolution of the Lebanese restraining bend of the Dead Sea
669 Transform. *Geological Society, London, Special Publications*, 135(1), pp.81-106.

- 670 Cartwright, J., Kirkham, C., Bertoni, C., Hodgson, N. and Rodriguez, K., 2018. Direct calibration of salt
671 sheet kinematics during gravity-driven deformation. *Geology*, 46(7), pp.623-626.
- 672 Cartwright, J. and Santamarina, C., 2015. Seismic characteristics of fluid escape pipes in sedimentary
673 basins: implications for pipe genesis. *Marine and Petroleum Geology*, 65, pp.126-140.
- 674 Cartwright, J., Jackson, M., Dooley, T. and Higgins, S., 2012. Strain partitioning in gravity-driven
675 shortening of a thick, multilayered evaporite sequence. Geological Society, London, Special
676 Publications, 363(1), pp.449-470.
- 677 Cartwright, J.A. and Jackson, M.P.A., 2008. Initiation of gravitational collapse of an evaporite basin
678 margin: The Messinian saline giant, Levant Basin, eastern Mediterranean. *Geological Society of
679 America Bulletin*, 120(3-4), pp.399-413.
- 680 Clark, I.R. and Cartwright, J.A., 2009. Interactions between submarine channel systems and
681 deformation in deepwater fold belts: Examples from the Levant Basin, Eastern Mediterranean sea.
682 *Marine and Petroleum Geology*, 26(8), pp.1465-1482.
- 683 Coleman, A.J., Jackson, C.A.L. and Duffy, O.B., 2017. Balancing sub-and supra-salt strain in salt-
684 influenced rifts: Implications for extension estimates. *Journal of Structural Geology*, 102, pp.208-225.
- 685 Cowie, P.A., 1998. A healing-reloading feedback control on the growth rate of seismogenic faults, J.
686 *Struct. Geol.*, 20, 1075–1087.
- 687 Cowie, P.A., Roberts, G.P., Bull, J.M. and Visini, F., 2012. Relationships between fault geometry, slip
688 rate variability and earthquake recurrence in extensional settings. *Geophysical Journal International*,
689 189(1), pp.143-160.
- 690 Davison, I., Alsop, I. and Blundell, D., 1996. Salt tectonics: some aspects of deformation mechanics.
691 Geological Society, London, Special Publications, 100(1), pp.1-10.
- 692 Dooley, T.P., Hudec, M.R., Carruthers, D., Jackson, M.P. and Luo, G., 2017. The effects of base-salt
693 relief on salt flow and suprasalt deformation patterns—Part 1: Flow across simple steps in the base of
694 salt. *Interpretation*, 5(1), pp.SD1-SD23.
- 695 Elfassi, Y., Gvirtzman, Z., Katz, O. and Aharonov, E., 2019. Chronology of post-Messinian faulting along
696 the Levant continental margin and its implications for salt tectonics. *Marine and Petroleum Geology*,
697 109, pp.574-588.
- 698 Evans, S.L. and Jackson, C.A.L., 2020a. Base-salt relief controls salt-related deformation in the Outer
699 Kwanza Basin, offshore Angola. *Basin Research*, 32(4), pp.668-687.
- 700 Evans, S. L., and Jackson, C.A.L., 2020b. Intrasalt Structure and Strain Partitioning in Layered
701 Evaporites: Implications for Drilling Through Messinian Salt in the Eastern Mediterranean. *EarthArXiv*.
702 DOI: 10.31223/osf.io/8pkbz.
- 703 Feng, Y.E., Yankelzon, A., Steinberg, J. and Reshef, M., 2016. Lithology and characteristics of the
704 Messinian evaporite sequence of the deep Levant Basin, eastern Mediterranean. *Marine
705 Geology*, 376, pp.118-131.
- 706 Feng, Y.E. and Reshef, M., 2016. The Eastern Mediterranean Messinian salt-depth imaging and velocity
707 analysis considerations. *Petroleum Geoscience*, 22(4), pp.333-339.

708 Feng, Y.E., Steinberg, J. and Reshef, M., 2017. Intra-salt deformation: Implications for the evolution of
709 the Messinian evaporites in the Levant Basin, eastern Mediterranean. *Marine and Petroleum Geology*,
710 88, pp.251-267.

711 Friedrich, A.M., Wernicke, B.P., Niemi, N.A., Bennett, R.A. & Davis, J.L., 2003. Comparison of geodetic
712 and geologic data from the Wasatch region, Utah, and implications for the spectral character of Earth
713 deformation at periods of 10 to 10 million years, *J. geophys. Res.*, 108, doi:10.1029/2001JB000682.

714 Gautier, F., G. Clauzon, J.P. Suc, J. Cravatte and D. Violanti, 1994, Age and duration of the Messinian
715 salinity crisis: *R. Acad. Sci., Paris (IIA)* 318, p. 1103–1109.

716 Gardosh, M.A. and Druckman, Y., 2006. Seismic stratigraphy, structure and tectonic evolution of the
717 Levantine Basin, offshore Israel. *Geological Society, London, Special Publications*, 260(1), pp.201-227.

718 Ghalayini, R., Daniel, J.M., Homberg, C., Nader, F.H. and Comstock, J.E., 2014. Impact of Cenozoic
719 strike-slip tectonics on the evolution of the northern Levant Basin (offshore Lebanon). *Tectonics*,
720 33(11), pp.2121-2142.

721 Ghalayini, R., Homberg, C., Daniel, J.M. and Nader, F.H., 2017. Growth of layer-bound normal faults
722 under a regional anisotropic stress field. *Geological Society, London, Special Publications*, 439(1),
723 pp.57-78.

724 Ghalayini, R., Nader, F.H., Bou Daher, S., Hawie, N. and Chbat, W.E., 2018. Petroleum systems of
725 Lebanon: an update and review. *Journal of Petroleum Geology*, 41(2), pp.189-214.

726 Gomez, F., Nemer, T., Tabet, C., Khawlie, M., Meghraoui, M. and Barazangi, M., 2007. Strain
727 partitioning of active transpression within the Lebanese restraining bend of the Dead Sea Fault
728 (Lebanon and SW Syria). *Geological Society, London, Special Publications*, 290(1), pp.285-303.

729 Gvirtzman, Z., M. Reshef, O. Buch-Leviatan and Z. Ben-Avraham, 2013, Intense salt deformation in the
730 Levant Basin in the middle of the Messinian salinity crisis: *Earth and Planetary Science Letters*, 379,
731 108–119.

732 Gvirtzman, Z., Manzi, V., Calvo, R., Gavrieli, I., Gennari, R., Lugli, S., Reghizzi, M. and Roveri, M., 2017.
733 Intra-Messinian truncation surface in the Levant Basin explained by subaqueous dissolution. *Geology*,
734 45(10), pp.915-918.

735 Hall, J., Calon, T.J., Aksu, A.E. and Meade, S.R., 2005. Structural evolution of the Latakia Ridge and
736 Cyprus Basin at the front of the Cyprus Arc, eastern Mediterranean Sea. *Marine Geology*, 221(1-4),
737 pp.261-297.

738 Hawie, N., Gorini, C., Deschamps, R., Nader, F.H., Montadert, L., Granjeon, D. and Baudin, F., 2013.
739 Tectono-stratigraphic evolution of the northern Levant Basin (offshore Lebanon). *Marine and
740 petroleum geology*, 48, pp.392-410.

741 Hudec, M.R. and Jackson, M.P., 2007. Terra infirma: Understanding salt tectonics. *Earth-Science
742 Reviews*, 82(1-2), pp.1-28.

743 Inati, L., Zeyen, H., Nader, F.H., Adelinet, M., Sursock, A., Rahhal, M.E. and Roure, F., 2016. Lithospheric
744 architecture of the Levant Basin (Eastern Mediterranean region): A 2D modeling approach.
745 *Tectonophysics*, 693, pp.143-156.

746 Jackson, M.P.A., B.C. Vendeville and D.D. Schultz-Ela, 1994, Structural dynamics of salt systems:
747 *Annual Review of Earth and Planetary Sciences*, 22(1), pp.93-117.

- 748 Jackson, M.P. and Hudec, M.R., 2005. Stratigraphic record of translation down ramps in a passive-
749 margin salt detachment. *Journal of Structural Geology*, 27(5), pp.889-911.
- 750 Jackson, M.P., Hudec, M.R., 2017. *Salt Tectonics: Principles and Practice*. Cambridge University Press.
- 751 Jones, I.F. and Davison, I., 2014. Seismic imaging in and around salt bodies. *Interpretation*, 2(4), pp.SL1-
752 SL20.
- 753 Kartveit, K.H., Omosanya, K.O., Johansen, S.E., Eruteya, O.E., Reshef, M. and Waldmann, N.D., 2018.
754 Multiphase structural evolution and geodynamic implications of Messinian salt-related structures,
755 levant basin, offshore Israel. *Tectonics*, 37(5), pp.1210-1230.
- 756 Kirkham, C., Cartwright, J., Bertoni, C., Rodriguez, K. and Hodgson, N., 2019. 3D kinematics of a thick
757 salt layer during gravity-driven deformation. *Marine and Petroleum Geology*, 110, pp.434-449.
- 758 Kirkham, C., Bertoni, C., Cartwright, J., Lensky, N.G., Sirota, I., Rodriguez, K. and Hodgson, N., 2020.
759 The demise of a 'salt giant' driven by uplift and thermal dissolution. *Earth and Planetary Science*
760 *Letters*, 531, p.115933.
- 761 Marton, L.G., Tari, G.C. and Lehmann, C.T., 2000. Evolution of the Angolan passive margin, West Africa,
762 with emphasis on post-salt structural styles. *Geophysical Monograph-American Geophysical Union*,
763 115, pp.129-150.
- 764 Matmon, A., Enzel, Y., Zilberman, E. and Heimann, A., 1999. Late Pliocene and Pleistocene reversal of
765 drainage systems in northern Israel: tectonic implications. *Geomorphology*, 28(1-2), pp.43-59.
- 766 McClymont, A.F., Villamor, P. & Green, A.G., 2009. Fault displacement accumulation and slip rate
767 variability within the Taupo Rift (New Zealand) based on trench and 3-D ground-penetrating radar
768 data, *Tectonics*, 28, TC4005, doi:10.1029/2008TC002334.
- 769 Meilijson, A., Hilgen, F., Sepúlveda, J., Steinberg, J., Fairbank, V., Flecker, R., Waldmann, N.D.,
770 Spaulding, S.A., Bialik, O.M., Boudinot, F.G. and Illner, P., 2019. Chronology with a pinch of salt:
771 Integrated stratigraphy of Messinian evaporites in the deep Eastern Mediterranean reveals long-
772 lasting halite deposition during Atlantic connectivity. *Earth-Science Reviews*.
- 773 Mitchell, S.G., Matmon, A., Bierman, P.R., Enzel, Y., Caffee, M. & Rizzo, D., 2001. Displacement history
774 of a limestone normal fault scarp, northern Israel, from cosmogenic ³⁶Cl, *J. geophys. Res.*, 106, 4247–
775 4264.
- 776 Mukherjee, S., Talbot, C.J. and Koyi, H.A., 2010. Viscosity estimates of salt in the Hormuz and
777 Namakdan salt diapirs, Persian Gulf. *Geological Magazine*, 147(4), pp.497-507.
- 778 Nader, F.H., Inati, L., Ghalayini, R., Hawie, N. and Daher, S.B., 2018. Key geological characteristics of
779 the Saida-Tyr Platform along the eastern margin of the Levant Basin, offshore Lebanon: implications
780 for hydrocarbon exploration. *Oil & Gas Science and Technology—Revue d'IFP Energies nouvelles*, 73,
781 p.50.
- 782 Netzeband, G.L., Hübscher, C.P. and Gajewski, D., 2006. The structural evolution of the Messinian
783 evaporites in the Levantine Basin. *Marine Geology*, 230(3-4), pp.249-273.
- 784 Nicol, A., Walsh, J., Berryman, K. & Villamor, P., 2006. Interdependence of fault displacement rates and
785 paleoearthquakes in an active rift, *Geology*, 34, 865–868.

786 Oppo, D, Evans, S, Iacopini, D, Kabir, SMM, Maselli, V, Jackson, CA-L., 2021. Leaky salt: Pipe trails
787 record the history of cross-evaporite fluid escape in the northern Levant Basin, Eastern
788 Mediterranean. Basin Research. <https://doi.org/10.1111/bre.12536>.

789 Peel, F.J., 2014. The engines of gravity-driven movement on passive margins: Quantifying the relative
790 contribution of spreading vs. gravity sliding mechanisms. Tectonophysics, 633, pp.126-142.

791 Pichel, L.M., Peel, F., Jackson, C.A. and Huuse, M., 2018. Geometry and kinematics of salt-detached
792 ramp syncline basins. Journal of Structural Geology, 115, pp.208-230.

793 Pichel, L.M., Jackson, C.A.L., Peel, F. and Dooley, T.P., 2019. Base-salt relief controls salt-tectonic
794 structural style, São Paulo Plateau, Santos Basin, Brazil. Basin Research, 32(3), pp.453-484.

795 Quirk, D.G., Schødt, N., Lassen, B., Ings, S.J., Hsu, D., Hirsch, K.K. and Von Nicolai, C., 2012. Salt
796 tectonics on passive margins: examples from Santos, Campos and Kwanza basins. Geological Society,
797 London, Special Publications, 363(1), pp.207-244.

798 Raith, A.F., Strozyk, F., Visser, J. and Urai, J.L., 2016. Evolution of rheologically heterogeneous salt
799 structures: a case study from the NE Netherlands. Solid Earth, 7(1), p.67.

800 Reiche, S., Hübscher, C. and Beitz, M., 2014. Fault-controlled evaporite deformation in the Levant
801 Basin, Eastern Mediterranean. Marine Geology, 354, pp.53-68.

802 Robinson, R., Nicol, A., Walsh, J.J. & Villamor, P., 2009. Features of earthquake recurrence in a complex
803 normal fault network: results from a synthetic seismicity model of the Taupo Rift, New Zealand, J.
804 geophys. Res., 114, B12306, doi:10.1029/2008JB006231.

805 Roveri, M., R. Flecker, W. Krijgsman, J. Lofi, S. Lugli, V. Manzi, F.J. Sierro, A. Bertini, A. Camerlenghi, G.
806 De Lange, R. Govers, F.J. Hilgen, C. Hübscher, P.T. Meijer, & M. Stoica, 2014, The Messinian salinity
807 crisis: Past and future of a great challenge for marine sciences: Marine Geology, 352, 25–58.

808 Rowan, M.G., Urai, J.L., Fiduk, J.C. and Kukla, P.A., 2019. Deformation of intrasalt competent layers in
809 different modes of salt tectonics. Solid Earth, 10(3), pp.987-1013.

810 Ryan, W.B.F., 2009, Decoding the Mediterranean salinity crisis: Sedimentology 56, 95–136.

811 Schlagenhauf, A., Gaudemer, Y., Benedetti, L., Manighetti, I., Palumbo, L., Schimmelpfennig, I., Finkel,
812 R. & Pou, K., 2010. Using in situ Chlorine-36 cosmonuclide to recover past earthquake histories on
813 limestone normal fault scarps: a reappraisal of methodology and interpretations, Geophys. J. Int., 182,
814 36–72, doi:10.1111/j.1365-246X.2010.04622.x.

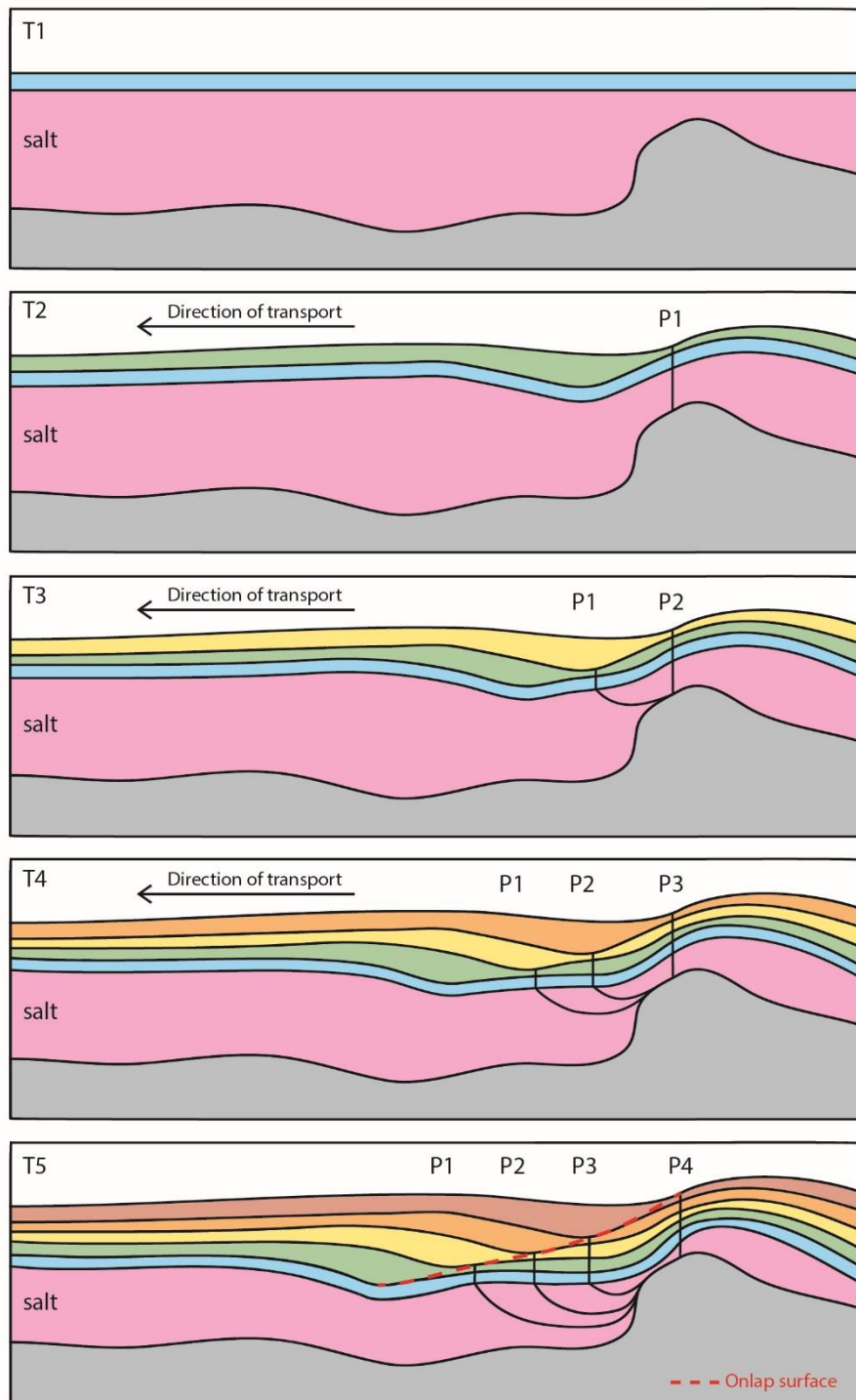
815 Schlagenhauf, A., Manighetti, I., Benedetti, L., Gaudemer, Y., Finkel, R., Malavieille, J.&Pou, K., 2011.
816 Earthquake supercycles in central Italy inferred from 36Cl exposure dating, Earth planet. Sci. Letts.,
817 307, 487–500, doi:10.1016/j.epsl.2011.05.022.

818 Schultz-Ela, D.D., 2001. Excursus on gravity gliding and gravity spreading. Journal of structural geology,
819 23(5), pp.725-731.

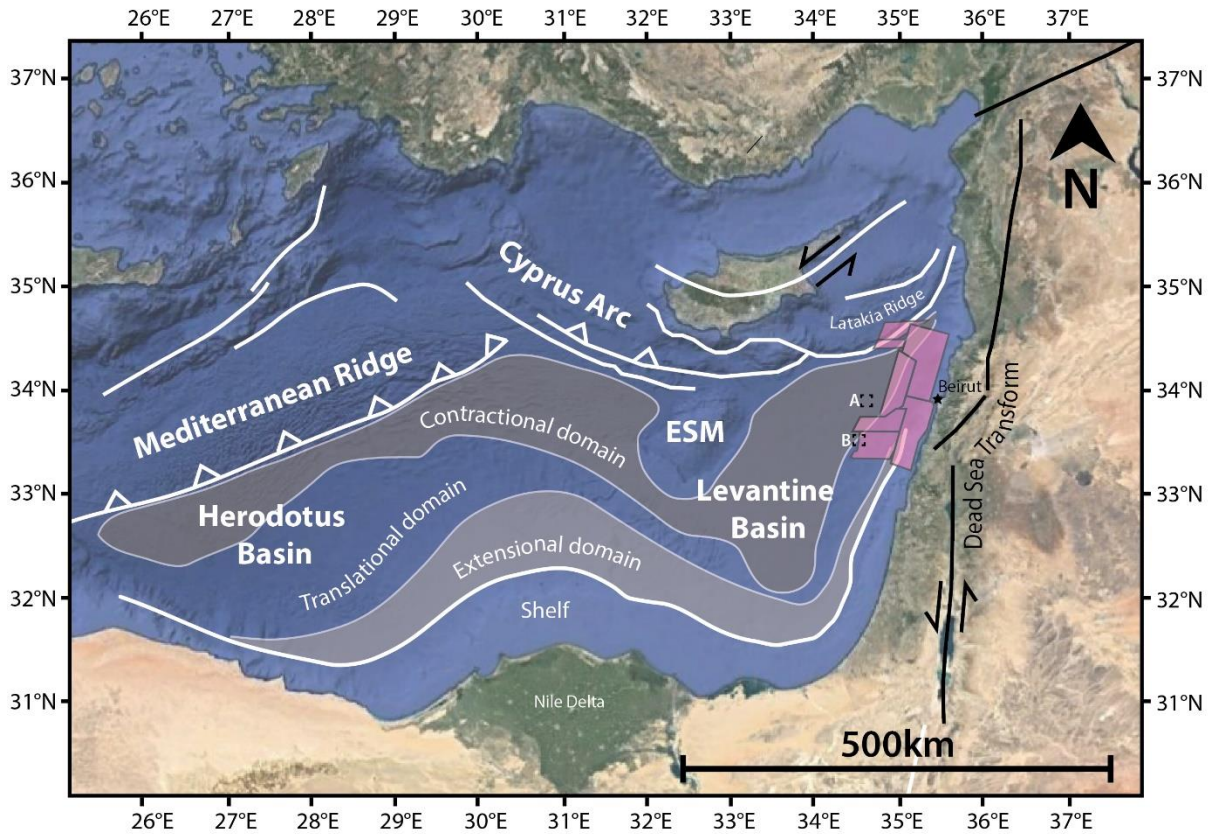
820 Spiers, C.J., Schutjens, P.M.T.M., Brzesowsky, R.H., Peach, C.J., Liezenberg, J.L. and Zwart, H.J., 1990.
821 Experimental determination of constitutive parameters governing creep of rocksalt by pressure
822 solution. Geological Society, London, Special Publications, 54(1), pp.215-227.

823 Urai, J.L., and Spiers, C.J., 2007. The effect of grain boundary water on deformation mechanisms and
824 rheology of rocksalt during long-term deformation, in Wallner, M., et al., eds., Proceedings of the 6th

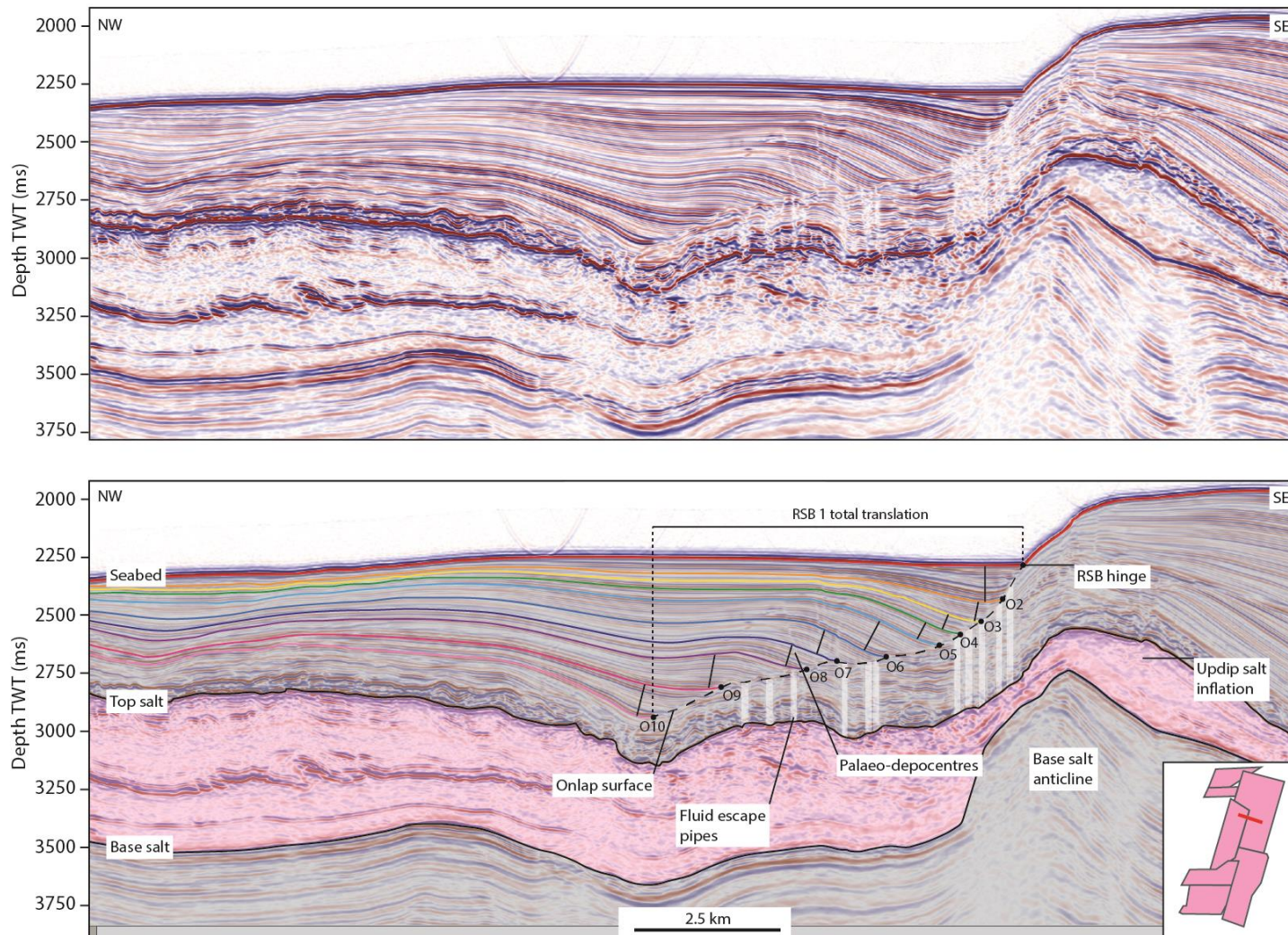
- 825 Conference on the Mechanical Behaviour of Salt: Understanding of THMC Processes in Salt Rocks:
826 London, Taylor and Francis, p. 149–158.
- 827 Urai, J.L., Schléder, Z., Spiers, C.J., and Kukla, P.A., 2008, Flow and transport properties of salt rocks,
828 in Littke, R., et al., eds., Dynamics of Complex Intracontinental Basins: The Central European Basin
829 System: Berlin, Heidelberg, Springer-Verlag, p. 277–290.
- 830 Van Keken, P.E., Spiers, C.J., Van den Berg, A.P. and Muzyert, E.J., 1993. The effective viscosity of
831 rocksalt: implementation of steady-state creep laws in numerical models of salt diapirism.
832 Tectonophysics, 225(4), pp.457-476.
- 833 Weijermars, R., Jackson, M.T. and Vendeville, B., 1993. Rheological and tectonic modeling of salt
834 provinces. Tectonophysics, 217(1-2), pp.143-174.



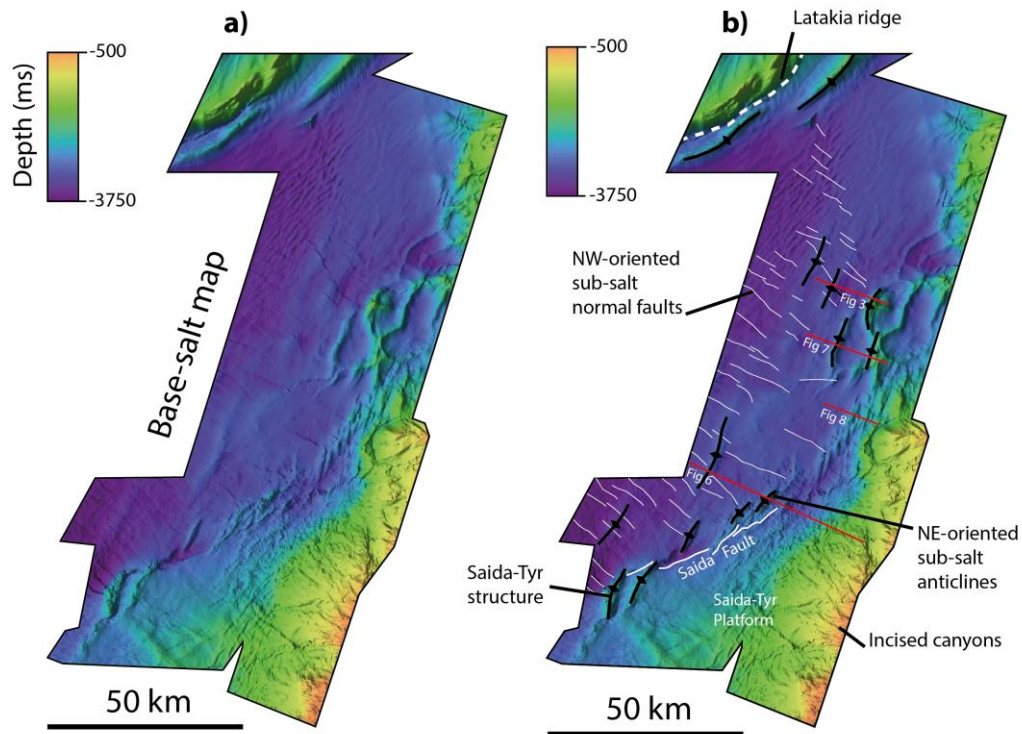
836 **Figure 1.** Schematic illustration of ramp syncline basin development and fluid escape pipes. Successive
 837 RSB depocentres and pipes are progressively translated away from their origin at the base-salt high.
 838 Growth strata filling the RSB depocentres create an 'onlap surface' in the stratigraphic record, with
 839 the horizontal distance from the oldest onlap to the sub-salt high giving the total magnitude of
 840 translation. Pipe age may be constrained by the age of the onlap that the terminus connects to at the
 841 base of the RSB.



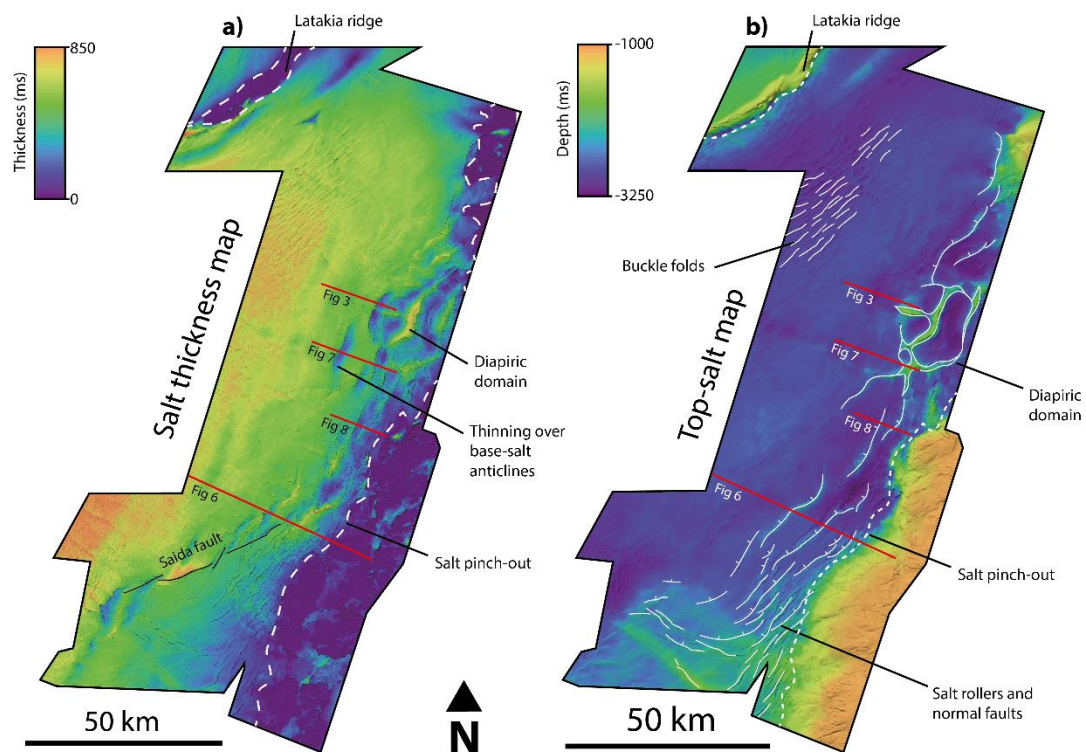
842 **Figure 2.** Location of dataset (pink polygons) and distribution of key tectonic elements in the Eastern
 843 Mediterranean. Boxes A and B denote location of previous studies of the Oceanus Structure
 844 (Cartwright et al., 2018) and the Saida-Tyr Structure (Kirkham et al., 2019), respectively. ESM =
 845 Eratosthenes Sea Mount. Modified from Allen et al., (2016).



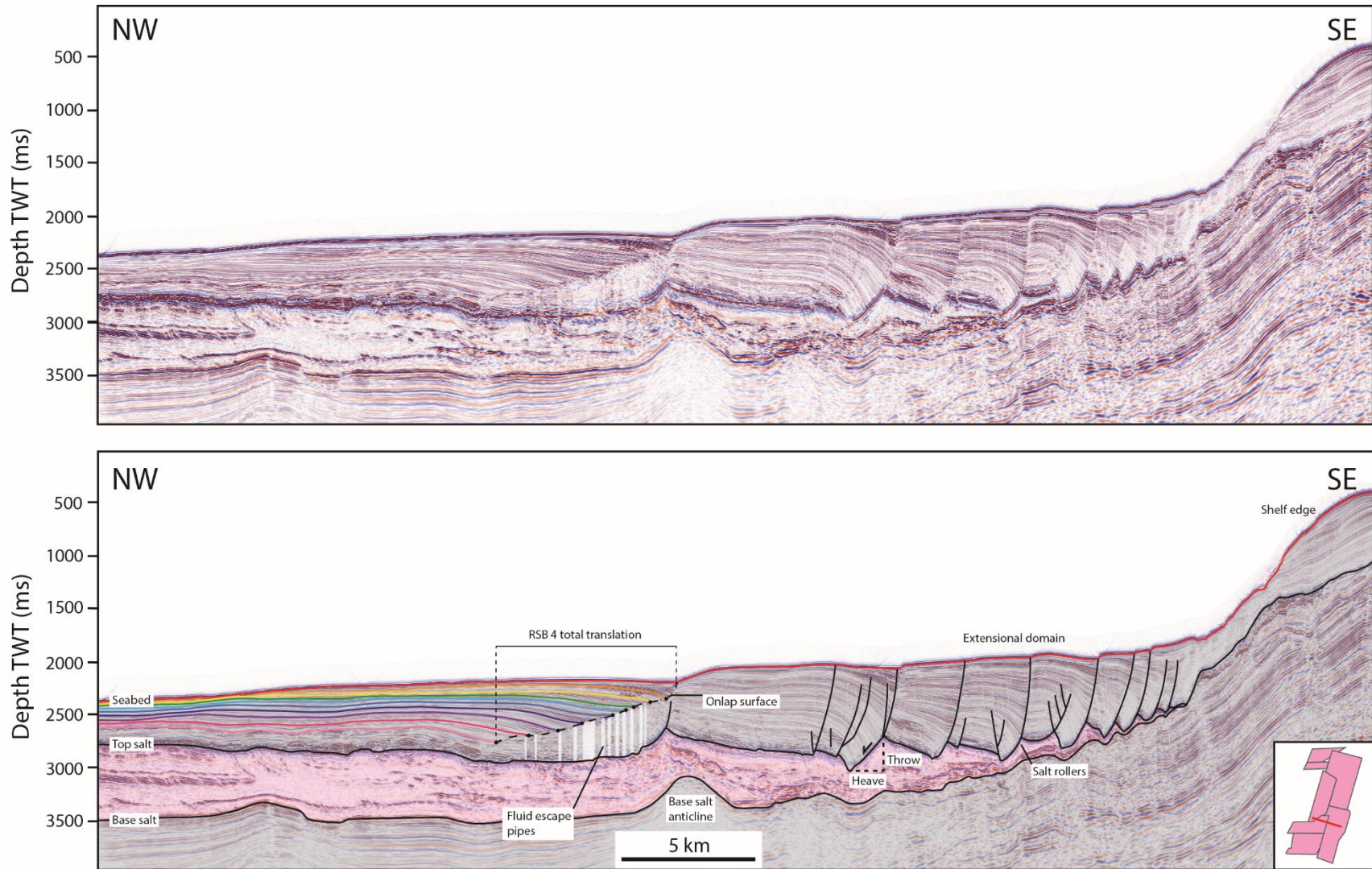
846 **Figure 3.** Seismic cross section showing base-salt anticline and associated ramp syncline basin downdip (RSB 1). Coloured lines show mapped intra-RSB
 847 horizons. Vertical white lines show fluid escape pipes. RSB depocentres form adjacent to the crest of the anticline and is subsequently translated downdip,
 848 preserving a stratigraphic record of downdip translation. Location of seismic line shown in inset map and in Figures 4 and 5.



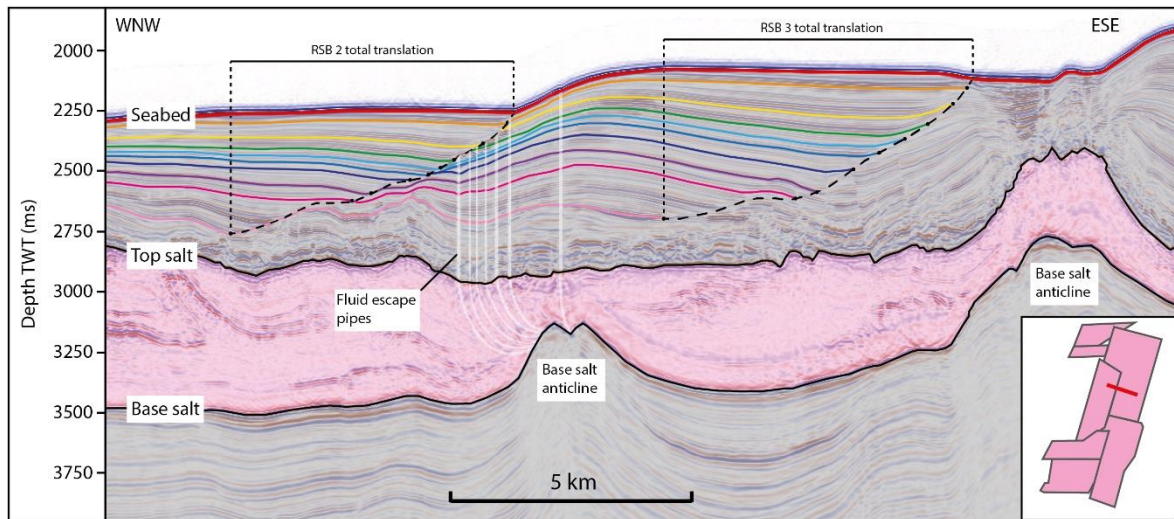
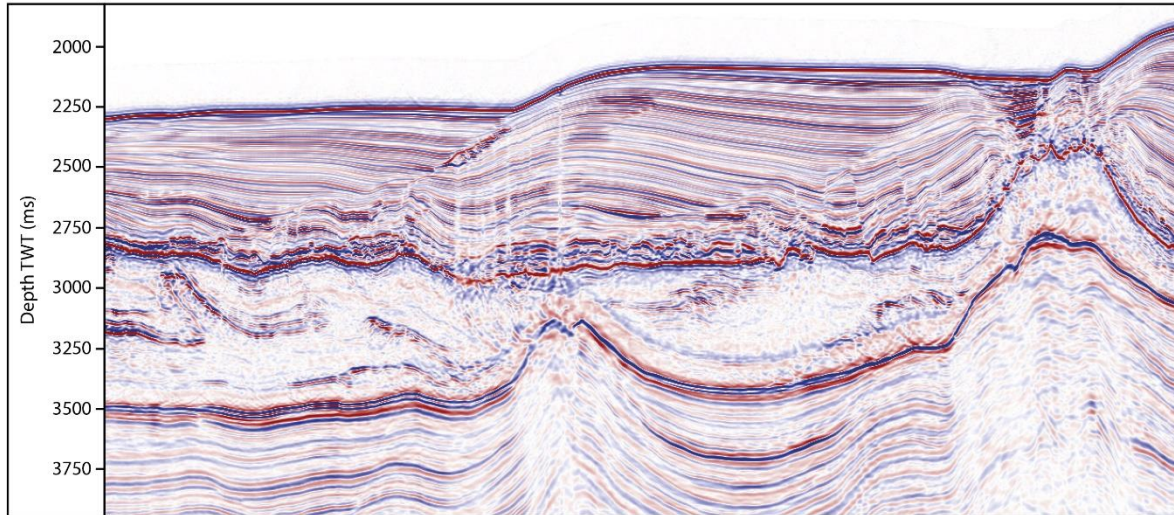
849 **Figure 4.** (a) Unannotated and (b) annotated TWT depth map of the base-salt surface showing the
 850 distribution of NE-trending anticlines (black) and NW-trending normal faults (white). Red lines show
 851 locations of seismic sections used in other figures.



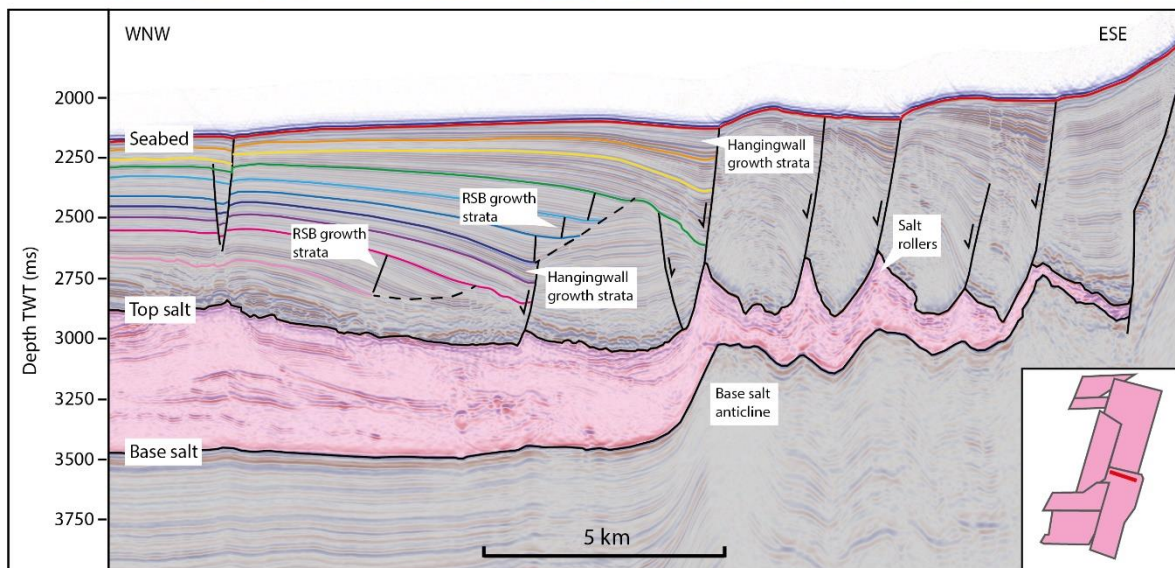
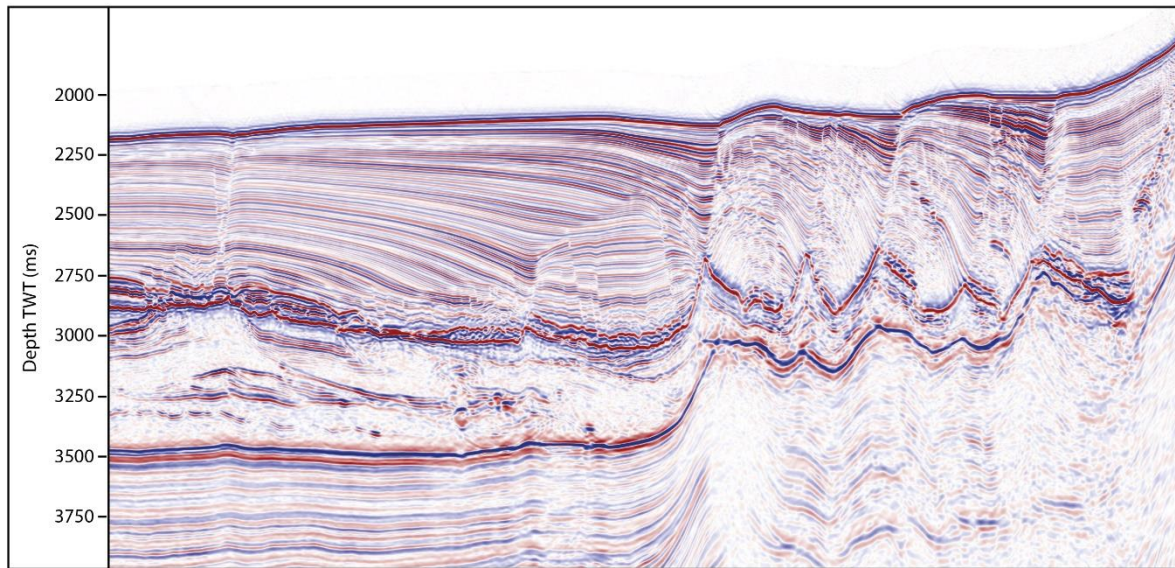
852 **Figure 5.** (a) Salt thickness map showing thinning over base-salt anticlines and pinch-out updip onto
 853 the Levant margin. (b) Top-salt depth map showing extensional structures along the margin and buckle
 854 folds around the Latakia Ridge. Red lines show locations of seismic sections used in other figures.



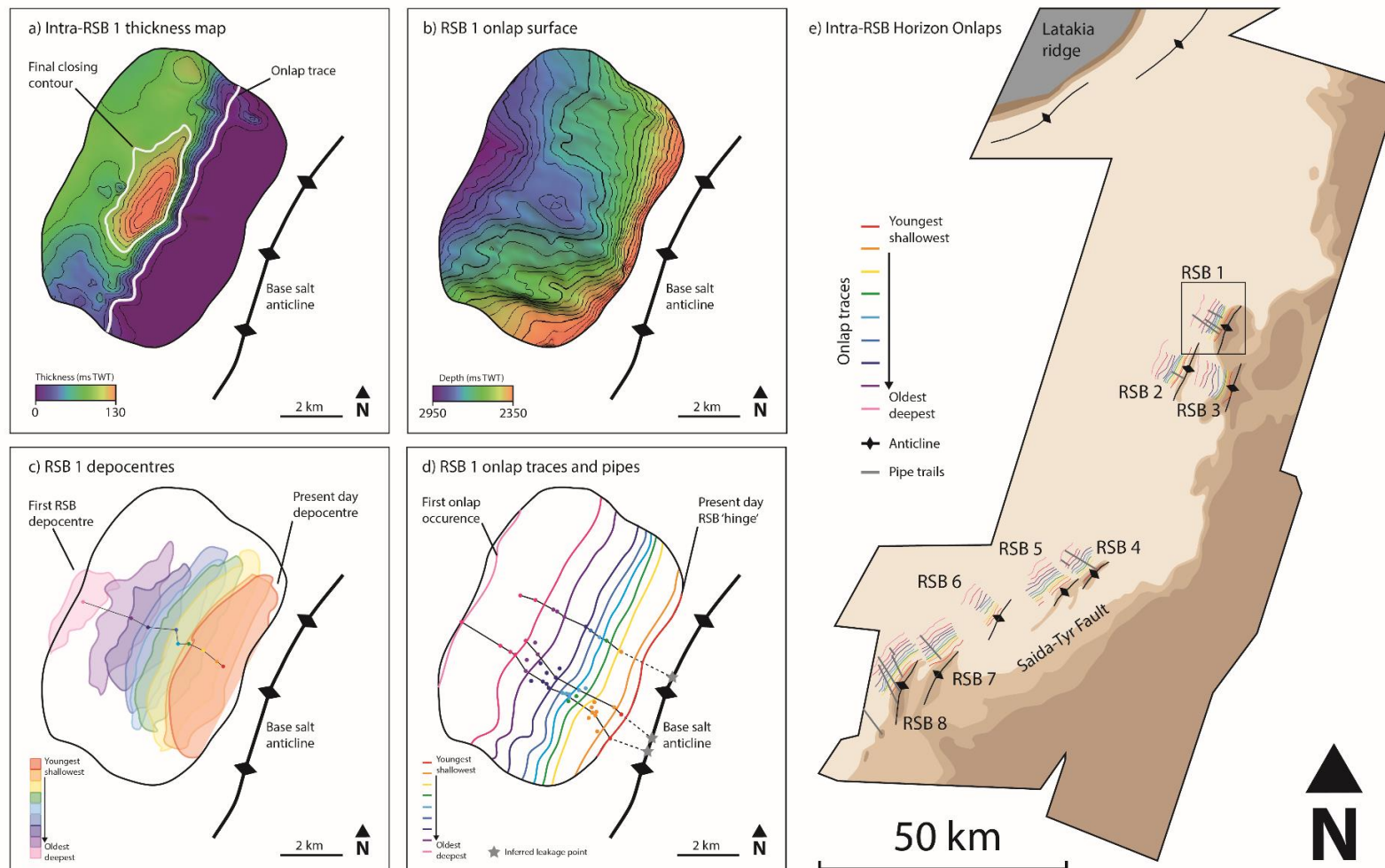
855 **Figure 6.** Seismic cross section showing thin-skinned extensional faults facilitating basinward translation of the overburden across the base-salt anticline.
 856 Coloured lines show mapped intra-RSB horizons. Vertical white lines show fluid escape pipes. Location of seismic line shown in inset map and in Figures 4 and 5.



857 **Figure 7.** Dual ramp syncline basins adjacent to parallel base-salt anticlines (basinward RSB 2 and
 858 landward RSB 3). Coloured lines show mapped intra-RSB horizons. Vertical white lines show fluid
 859 escape pipes. Location of seismic line shown in inset map and in Figures 4 and 5.

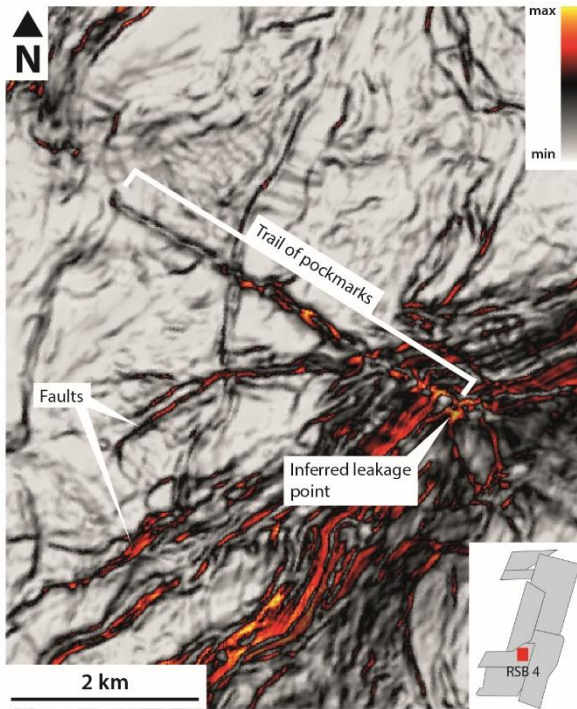


860 **Figure 8.** Disrupted RSB development due to intermittent normal faulting. Packages of RSB growth
 861 strata and hangingwall growth strata indicate phases of continuous translation and phases of faulting.
 862 Coloured lines show mapped intra-RSB horizons. Location of seismic line shown in inset map and in
 863 Figures 4 and 5.

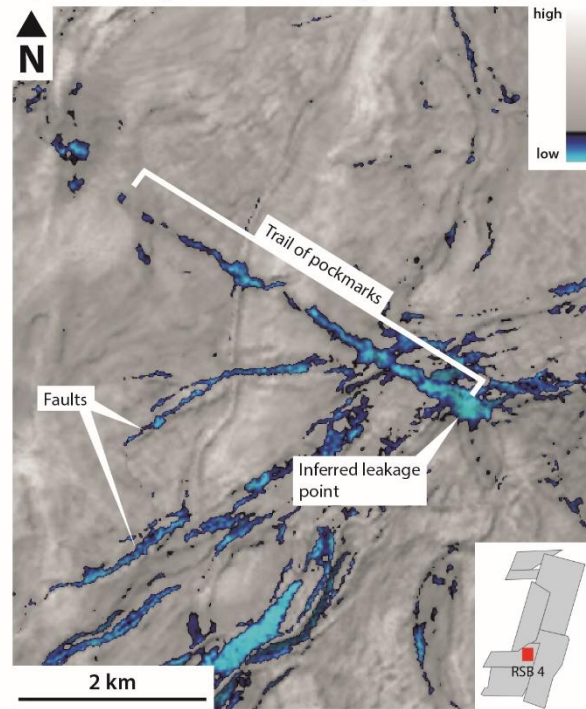


864 **Figure 9.** (a) Example thickness map of intra-RSB unit showing final closing contour and onlap trace. (b) Geometry of the onlap surface. (c) Stacked RSB
865 depocentre outlines showing their migration away from the anticline with increasing age. Tracing the thickest succession of each unit gives the direction of
866 translation. (d) Mapped onlap traces for RSB 1 and fluid escape pipe trails coloured by age of corresponding intra-RSB unit. (e) Distribution of base-salt
867 anticlines and mapped onlap traces for RSBs presented in this study. Grey lines show associated pipe trails. Square indicates location of (a-d). Shade of brown
868 corresponds to depth of base-salt (lighter = deeper).

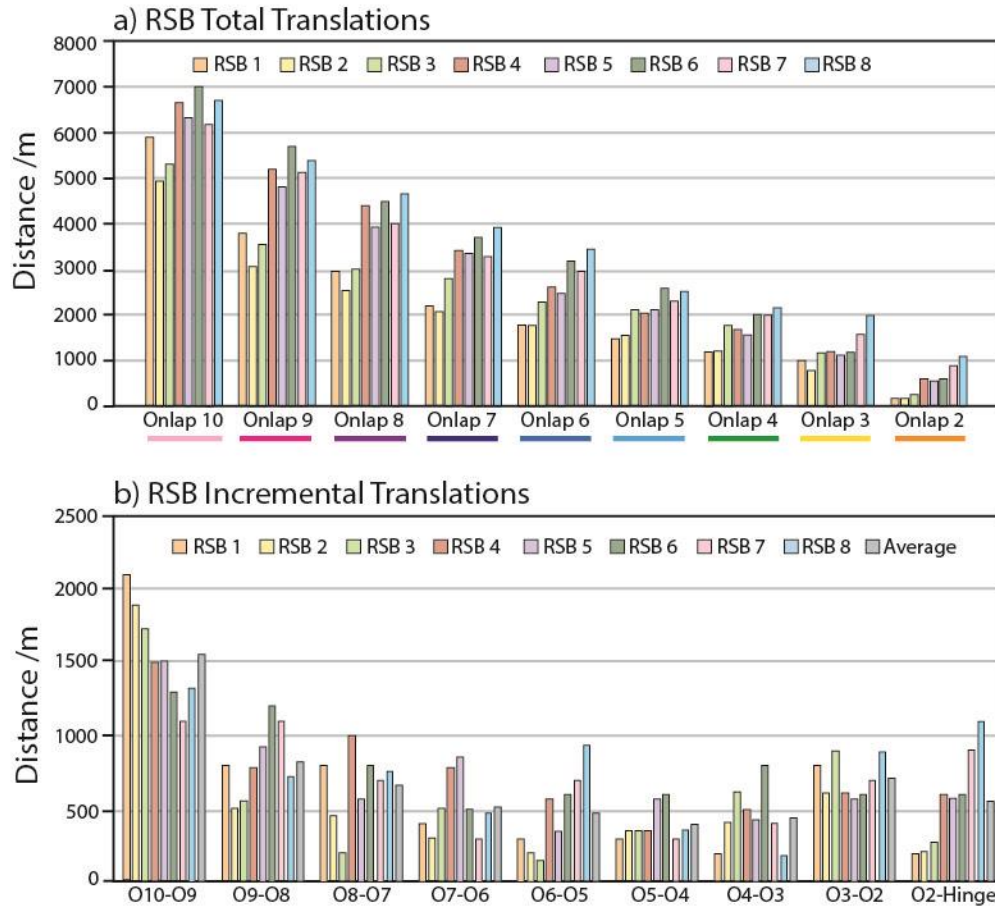
a) RSB 4 top salt variance map



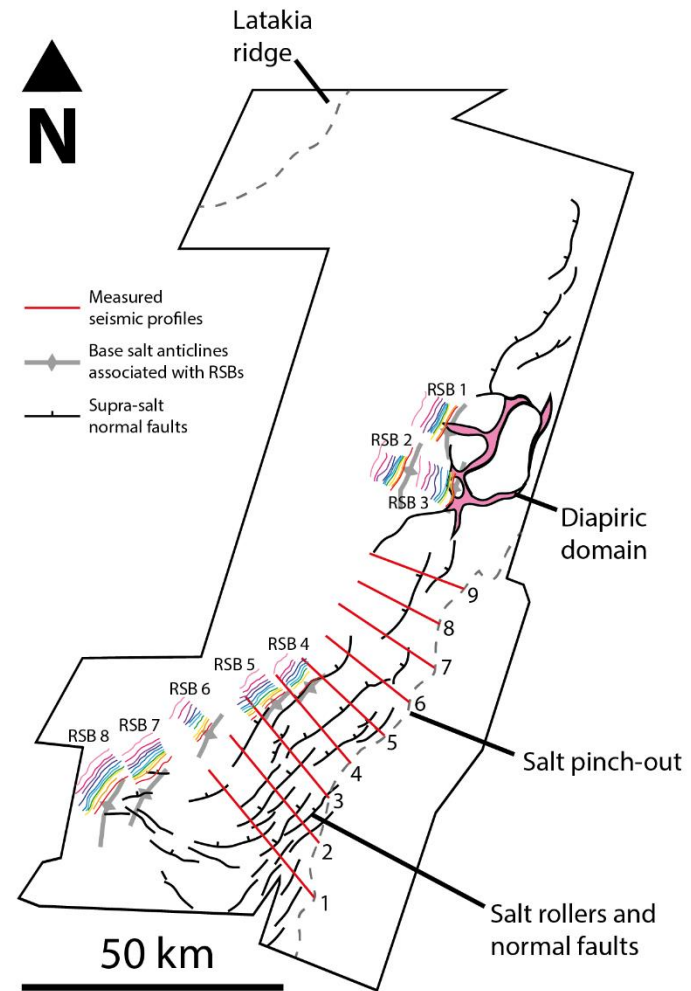
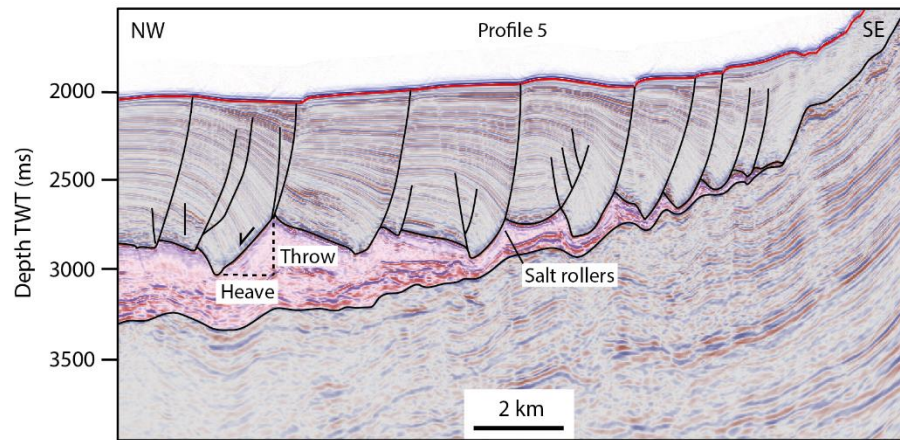
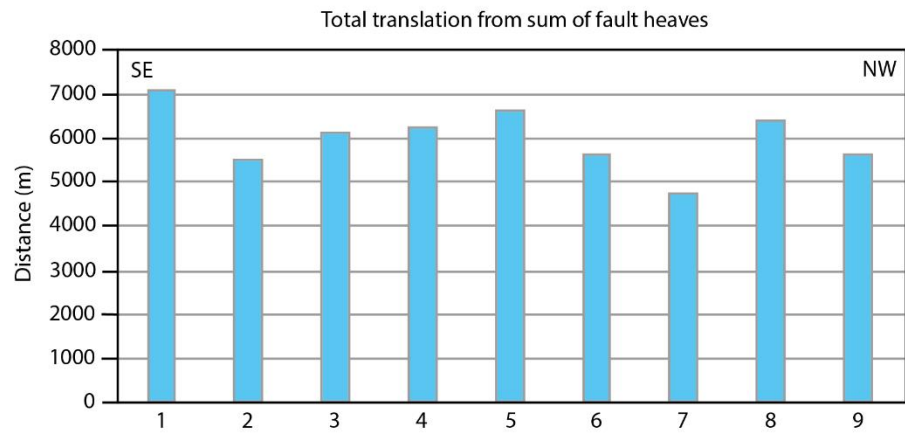
b) RSB 4 top salt RMS amplitude map



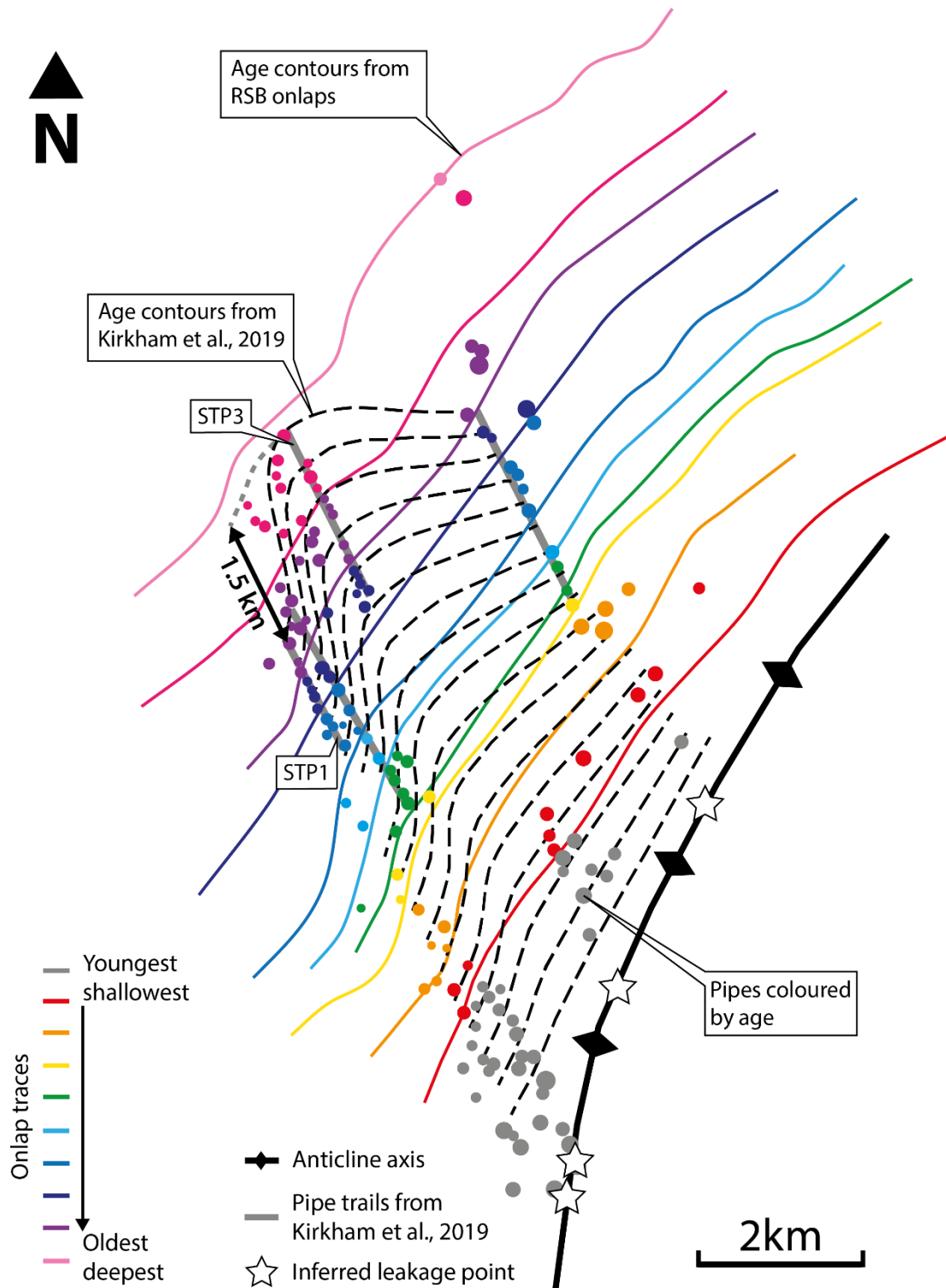
869 **Figure 10.** Variance (a) and RMS amplitude (b) maps of the top-salt surface showing the RSB 4 pipe
870 trail. Location of RSB 4 shown in inset and seismic cross section through pipe trail shown in Figure 6.



871 **Figure 11.** (a) Magnitudes of translation measured for intra-RSB onlaps of equivalent ages in each RSB.
 872 The magnitude of translation given by the oldest onlap (Onlap 10) represents the total translation
 873 experienced by each RSB. (b) Magnitudes of translation during different time periods, given by the
 874 differences between total onlap translations. O10-O9 represents the oldest increment of time, with
 875 O2-Hinge representing the most recent increment of time.

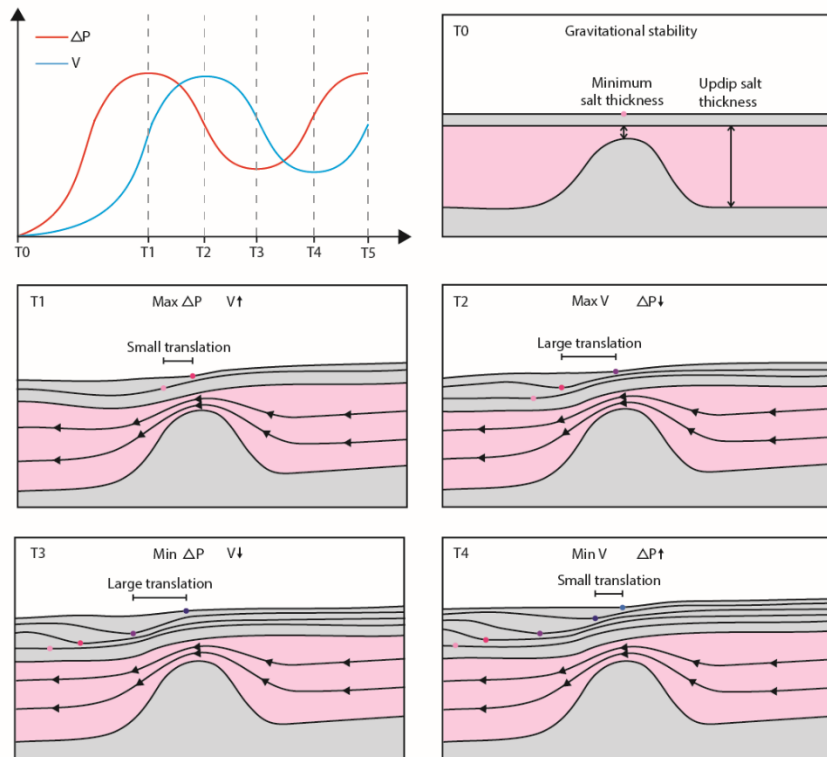


876 **Figure 12.** Plot of total translation magnitudes calculated from summing the heaves (horizontal components of fault slip) of normal faults in the updip
 877 extensional domain. Red lines show locations of measured seismic profiles. Coloured lines show locations of RSB onlap traces for reference.

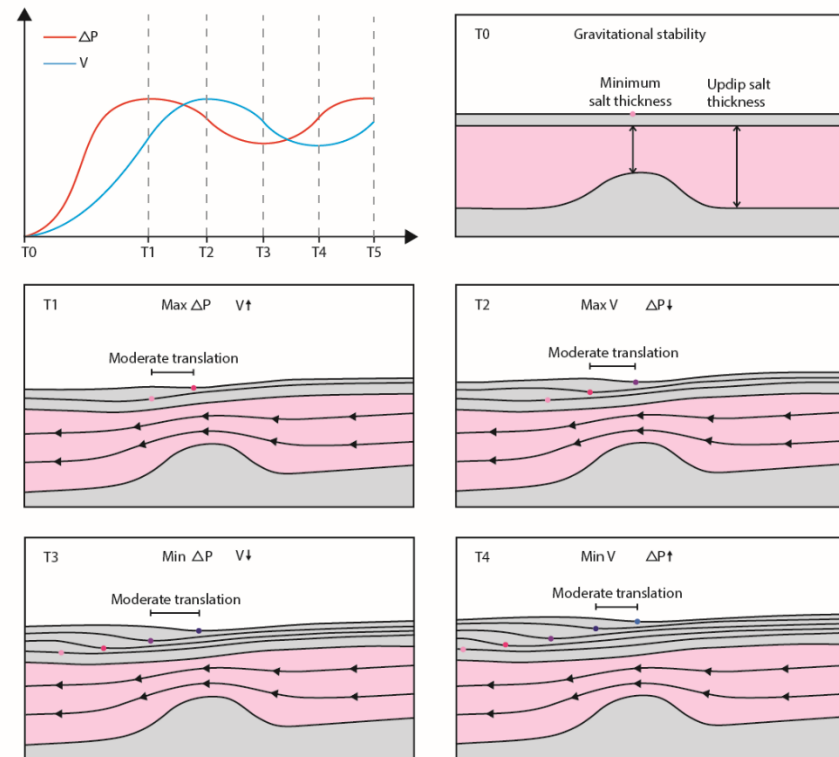


878 **Figure 13.** Coloured lines show age contours given by onlap traces for RSB 8. Pipes coloured by age of
 879 corresponding intra-RSB unit. Dashed lines show age contours inferred by Kirkham et al., (2019)
 880 assuming equivalent age of first pipe in each trail. Sub-parallel onlap traces show uniform translation
 881 away from the base-salt anticline.

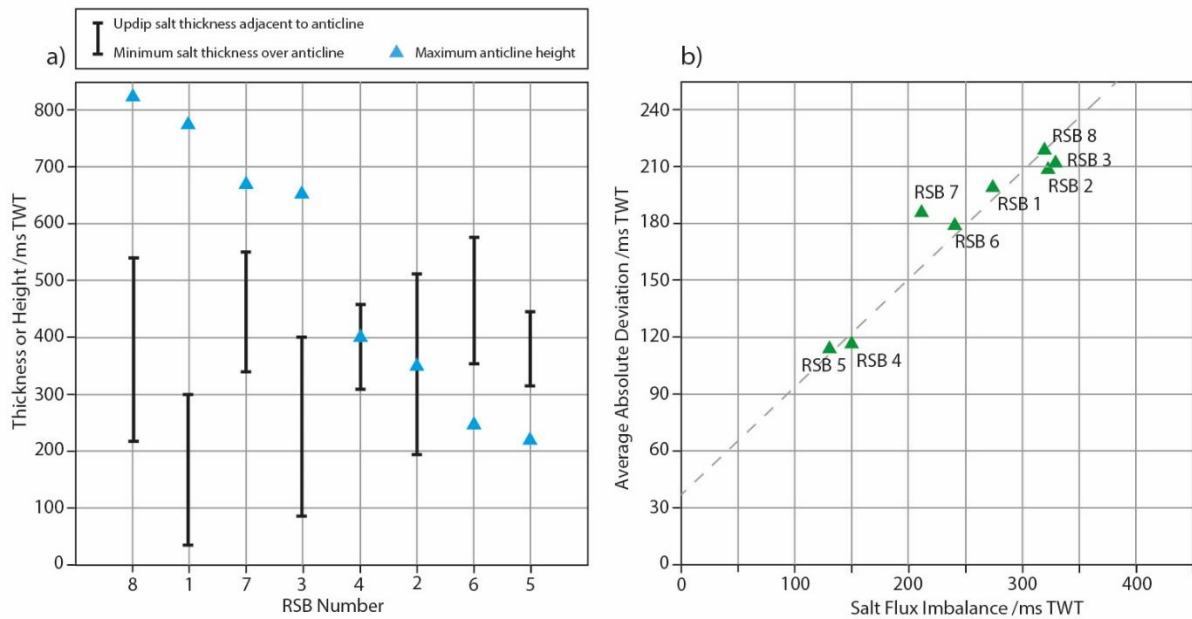
a) Large salt flux imbalance



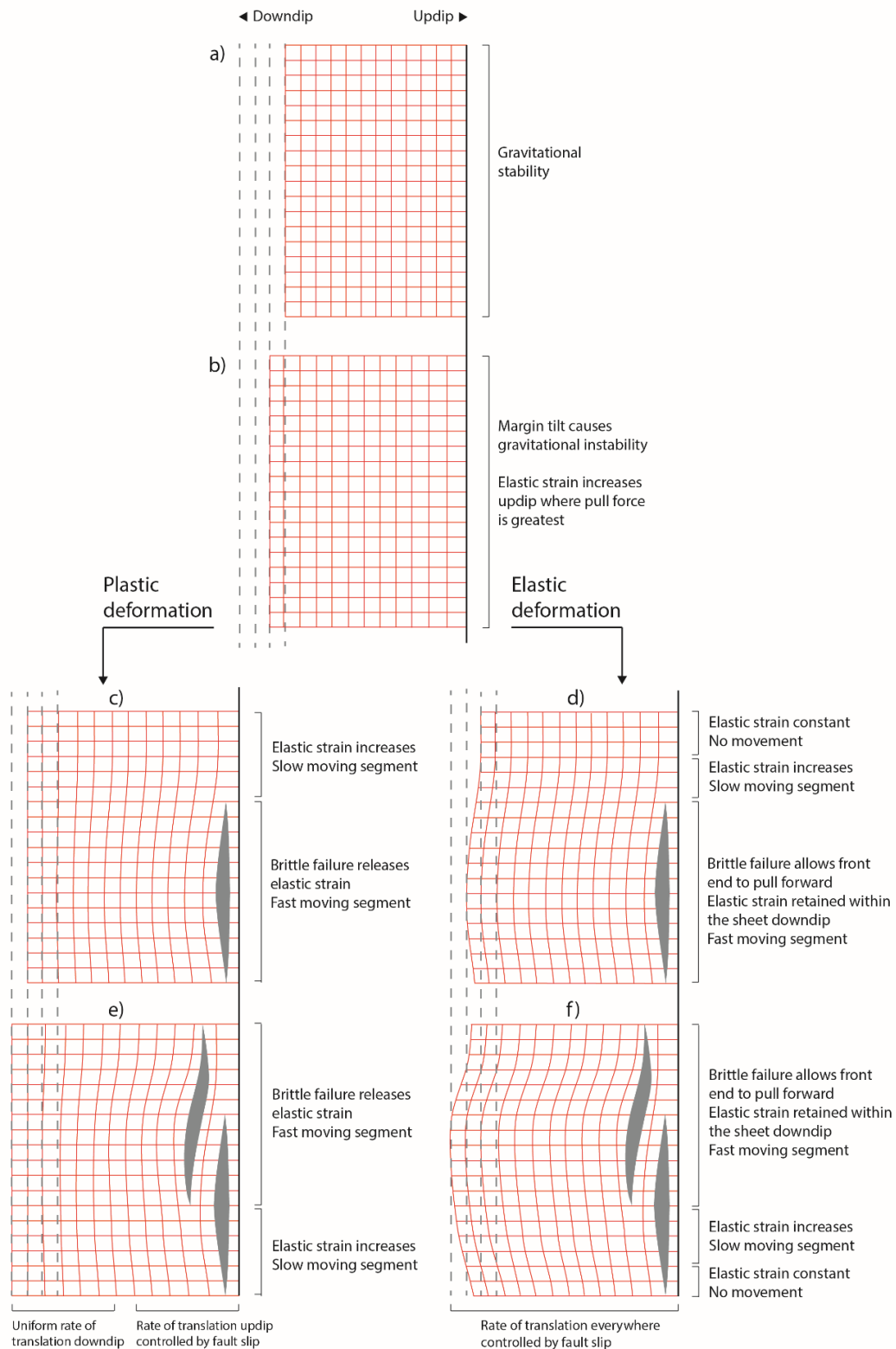
b) Small salt flux imbalance



882 **Figure 14.** Schematic showing time-varying evolution of pressure and velocity during salt flow over a base-salt anticline. In the first instance, pressure builds
 883 within the salt on the updip flank due to the volumetric mismatch (more salt input than output). This process gradually increases the pressure difference (ΔP)
 884 across the anticline (T0-T1). In turn, this pressure difference increases the stress acting upon the salt, and since stress is proportional to strain rate, the velocity
 885 of salt flow across the anticline increases (T0-T1). The acceleration of the salt flow is proportional to the pressure difference across the anticline, such that
 886 maximum acceleration occurs when ΔP is at its peak (T1). This velocity increase reduces the volumetric imbalance across the anticline and allows the pressure
 887 difference across the anticline to drop (T1-T2). As the system approaches equilibrium, the stress acting on the salt is reduced and it begins to decelerate (T2-T3). The pressure
 888 difference across the anticline then starts to build up again, and the process repeats (T3-T4). The feedback between pressure difference and velocity therefore
 889 causes them to vary in a cyclical nature. Pressure and velocity variations are more extreme for a large salt flux imbalance (a) than a small salt flux imbalance
 890 (b).



891 **Figure 15.** (a) Plot of anticline height, adjacent salt thickness and minimum salt thickness over the
 892 crest for each RSB, ordered from largest to smallest anticline height. The difference between adjacent
 893 updip salt thickness and minimum thickness over the crest is a proxy for the magnitude of salt flux
 894 imbalance. (b) The average absolute deviation of each RSB is proportional to its salt flux imbalance.
 895 This means that RSBs with a large salt flux imbalance show more extreme variability in relative
 896 translation rate with respect to the average at each time interval than those with a small salt flux
 897 imbalance. The R^2 value for this correlation is 0.9.



898 **Figure 16** Schematic showing two end-member models for elastic strain build-up and release within
 899 the overburden. A dominantly plastic overburden allows the translational domain to pull away at a
 900 uniform rate and the faults in the updip domain rupture as and when they reach a critical stress, locally
 901 releasing the elastic strain build-up. A dominantly elastic overburden remains under tension and the
 902 ruptures updip allow the sheet to pull forward by a magnitude dictated by the fault slip. The actual
 903 behaviour of the overburden at the margin-scale is modelled as an elasto-plastic sheet and therefore
 904 a hybrid of these two end-members.